Editors' Suggestion

Bridging Hubbard model physics and quantum Hall physics in trilayer graphene/*h*-BN moiré superlattice

Ya-Hui Zhang and T. Senthil
Department of Physics, Massachusetts Institute of Technology, Cambridge, Massachusetts 02139, USA

(Received 4 December 2018; revised manuscript received 22 March 2019; published 28 May 2019)

The moiré superlattice formed by ABC stacked trilayer graphene aligned with a hexagonal boron nitride substrate (TG/h-BN) provides an interesting system where both the bandwidth and the topology can be tuned by an applied perpendicular electric field D. Thus the TG/h-BN system can simulate both Hubbard model physics and nearly flat Chern band physics within one sample. We derive lattice models for both signs of D (which controls the band topology) separately through explicit Wannier orbital construction and mapping of Coulomb interaction. When the bands are topologically trivial, we discuss possible candidates for Mott insulators at integer number of holes per site (labeled as ν_T). These include both broken symmetry states and quantum spin liquid insulators which may be particularly favorable in the vicinity of the Mott transition. We propose feasible experiments to study carefully the bandwidth tuned and the doping tuned Mott metal-insulator transition at both $\nu_T = 1$ and $\nu_T = 2$. We discuss the interesting possibility of probing experimentally a bandwidth (or doping) controlled continuous Mott transition between a Fermi liquid metal and a quantum spin liquid insulator. Finally we also show that the system has a large valley Zeeman coupling to a small out-of-plane magnetic field, which can be used to control the valley degree of freedom.

DOI: 10.1103/PhysRevB.99.205150

I. INTRODUCTION

Recently moiré superlattices in twisted Van der Waals heterostructures have been shown to realize several strongly correlated systems with high tunability [1–5]. Correlated insulators and superconductors have been reported experimentally in twisted bilayer graphene [2,3,5] and in ABC stacked graphene/hexagonal boron nitride (TG/h-BN) [4]. In this paper, we focus on the TG/h-BN system.

A bandwidth [4] and even band topology [6] can be tuned by an applied perpendicular electric field D in TG/h-BN. The displacement field D provides an energy difference Δ_V for electrons between the top and the bottom graphene layer, as illustrated in Fig. 1. For $\Delta_V < 0$ (this convention assumes that the h-BN layer on top is nearly aligned with the TG), the bands of the two valleys have zero Chern number, while for $\Delta_V > 0$, they have nonzero Chern numbers $C = \pm 3$ [6,7]. Correlated insulators are found at $\nu_T = 1$ and $\nu_T = 2$ for the valence band of TG/h-BN at large $|\Delta_V|$ [4], where ν_T is defined as the total density of holes per moiré unit cell. When $\Delta_V > 0$, physics similar to quantum Hall systems may be realizable. For trivial narrow bands that obtain when $\Delta_V < 0$, the physics is expected [8] to be governed by an anisotropic SU(4) Hubbard model (with small anisotropies) at leading order. Therefore TG/h-BN offers an experimental system where both Hubbard model physics and quantum Hall like physics can be simulated by simply switching the gate.

In this paper, we describe several new aspects of the physics of TG/h-BN with a focus on the topologically trivial side ($\Delta V < 0$). We obtain an explicit interacting lattice model and estimate its parameters using the continuum description of the moiré band structure [9]. We use this lattice model to discuss the physics both deep in the correlated insulator regime and in the regime close to the Mott metal-insulator transition. We highlight the opportunities presented by this system to tunably study both the bandwidth tuned and doping tuned Mott transitions. We propose a number of transport experiments that can probe the Mott transition. We also present some new results on the topological bands that obtain for $\Delta_V > 0$.

For $\Delta_V < 0$, we build Wannier orbitals following the standard approach, and explicitly construct an effective tight-binding model. We project the Coulomb interactions to determine the effective interactions in the lattice model. The result is a spin-valley extended Hubbard model with Hund's couplings as much smaller perturbations. The SU(4) symmetry from the spin-valley degrees of freedom is mainly broken by a valley-contrasting flux in the hopping. Based on this model, we argue that the insulators found in the experiment should be understood as standard Mott insulators with charge frozen by Hubbard U, in contrast to the nesting scenario in Ref. [10]. In the limit of a nearly flat band, we argue that the insulator should be a *ferromagnet* for both $\nu_T = 1$ and $\nu_T = 2$. For intermediate strength interactions, quantum spin liquids phases are promising candidates. In the vicinity of the Mott transition, a natural candidate is a spin liquid with neutral Fermi surface coupled to an emergent U(1) gauge field.

The Mott metal-insulator transition [11] is a fundamental phenomenon in condensed matter physics. Graphene moiré systems like TG/h-BN offer a wonderful opportunity to controllably tune through the transition and explore its properties. It has long been appreciated that there are a number of distinct routes to the Mott transition in correlated solids. We describe distinctive signatures—visible in feasible experiments on TG/h-BN—of some of these distinct routes. Most striking is

 ©2019 American Physical Society

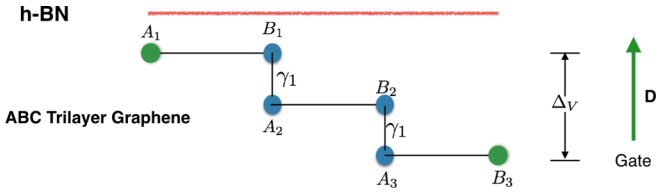

FIG. 1. Illustration of the ABC stacked trilayer graphene/h-BN system. We assume the h-BN layer on top is nearly aligned with the graphene layers. A and B refer to the two sublattices in each of the graphene layers. Due to the large dimerization term $\gamma_1 \approx 400$ meV, only A_1 and B_3 should be kept at low energy, forming a two-component spinor. A vertical electric field gives an energy difference Δ_V for electrons between the top and the bottom graphene layers. The aligned h-BN layer provides a moiré superlattice potential which folds the original large Brillouin zone to a small moiré Brilloiun zone (MBZ).

the possibility [12] of a bandwidth tuned continuous quantum critical Mott transition from the Fermi liquid metal to a spin liquid with a neutral Fermi surface. We show how to explore such a continuous Mott transition through simple transport experiments: a universal jump of residual resistivity at the critical point and Shubnikov-deHaas oscillations even inside the Mott insulator. Besides, we also discuss the possibility of a doping controlled continuous metal-insulator transition (DMIT) between the above two phases. Interestingly we find that the existing experimental data in Ref. [4] may already have signatures of such a doping tuned continuous metal-insulator transition close to the filling $\nu_T = 2$.

Finally, we show that there is a large valley Zeeman coupling with averaged g factor $g \sim 54$. Therefore a small out of plane magnetic field can polarize the valley and lead to a spin 1/2 model. We discuss some consequences of this phenomenon.

For the topologically nontrivial $\Delta_V > 0$ side, valley preserving localized Wannier orbitals are impossible because of the nonzero Chern number $C = \pm 3$. Related but distinct Wannier obstructions have also been discussed in the context of the twisted bilayer graphene system [8,13–15]. The Wannier obstruction for the $\Delta_V > 0$ TG/h-BN system can not be removed by adding trivial bands and is therefore different from the fragile topology of the twisted bilayer graphene system [16]. Following a similar treatment of twisted bilayer graphene in Ref. [8], we build a two-orbital model on the triangular lattice, though the valley charge operator is not a sum of on-site terms. As argued in our previous work [6], the $\Delta_V > 0$ side is promising to realize a quantum anomalous Hall insulating state with strong interactions at $\nu_T = 1$. At fractional fillings, fractional quantum anomalous Hall states may also be possible. The model derived in the present paper may in the future aid quantitative theoretical and numerical studies of these phenomena.

II. LATTICE MODEL FOR $\Delta_V < 0$ SIDE: SPIN-VALLEY HUBBARD MODEL

Band structures of TG/h-BN were calculated in Ref. [6] using a continuum model. An important feature, as demonstrated experimentally in Ref. [4], is that the bandwidth can simply be tuned by the perpendicular displacement field D (equivalently the potential difference Δ_V). More details of the band structure can be found in Appendix A. Here we will use the results on the band structure to build an interacting lattice model with a focus on the topologically trivial $\Delta_V < 0$ side.

When $\Delta_V < 0$, the valence band of each valley has zero Chern number and exponentially localized Wannier orbital on triangular lattice can be constructed for each valley separately. Following the methods in Appendix C, we derived an interacting triangular lattice model which we describe below. At each site $\mathbf{x}$ of the lattice, there are four single-particle states corresponding to two spin and two valley degrees of freedom. We work in the hole picture. We write the corresponding hole destruction operator as $\psi_{a,\sigma}(\mathbf{x})$, where $a = \pm$ is the valley index and $\sigma = \uparrow, \downarrow$ is the spin index.

Microscopically the system has symmetries of charge conservation, spin rotation, and time reversal. The latter acts by flipping the two valleys:[1]

$$\mathcal{T} : \psi_{a,\sigma}(\mathbf{x}) \to (\tau^x)_{ab}\psi_{b,\sigma}(\mathbf{x}). \tag{1}$$

For a large period moiré structure, (super)lattice translations are an excellent symmetry as is a C_3 rotation (about a triangular site), which acts as

$$\mathcal{C}_3 : \psi_{a,\sigma}(\mathbf{x}) \to \psi_{a,\sigma}(\mathbf{x}'), \tag{2}$$

where $\mathbf{x}'$ is the site to which $\mathbf{x}$ is taken by the C_3 rotation. Further, to an excellent approximation, the number of electrons within each valley is independently conserved. There is a corresponding valley charge U(1) symmetry. Finally within the continuum model there is a mirror reflection symmetry which also interchanges the two valleys (see Appendix A):

$$\mathcal{M} : \psi_{a,\sigma}(\mathbf{x}) \to (\tau^x)_{ab}\psi_{b,\sigma}(\mathbf{x}') \tag{3}$$

where $\mathbf{x}'$ is generated from $\mathbf{x}$ by a mirror reflection plane passing through $\mathbf{a_1} + \mathbf{a_2}$, where $\mathbf{a_1} = a_M(1, 0)$ and $\mathbf{a_2} = a_M(\frac{1}{2}, \frac{\sqrt{3}}{2})$ are two unit vectors for the triangular lattice.

Note that there is no microscopic C_6, and hence C_2 symmetry. If present, C_2T will forbid any nonzero Berry curvature at generic points in the MBZ. However, there exist nonzero Berry curvature close to the Γ point and the MBZ boundary [6] though their sum cancels for the $\Delta_V < 0$ side. In the next section, we will also show that there is a large out of plane orbital magnetic moment $\mathbf{m}(\mathbf{k})$ at each momentum $\mathbf{k}$, which can not be compatible with the existence of both time-reversal and C_6 symmetry.

Below we will derive a lattice model for the active bands. In the noninteracting limit, despite its absence as a microscopic symmetry, the lattice tight-binding model is symmetric under a C_6 rotation (about a triangular site) which acts as

$$\mathcal{C}_6 : \psi_{a,\sigma}(\mathbf{x}) \to (\tau^x)_{ab}\psi_{b,\sigma}(\mathbf{x}'), \tag{4}$$

where $\mathbf{x}'$ is the site to which $\mathbf{x}$ is taken by the C_6 rotation. Thus C_6 flips the two valleys. This symmetry will be broken by interaction terms. However we will see that the part of

[1]It is convenient to define time reversal without flipping the spin. We are free to combine this with a spin rotation to obtain a modified time-reversal operation which flips both spin and valley.

TABLE I. Tight-binding parameters for $\Delta_V < 0$ side. Both Δ_V and t are in units of meV.

Δ_V	t_1	t_2	t_3	t_4
-100	$1.505e^{i0.780\pi}$	-0.063	$0.046e^{-i0.544\pi}$	$0.323e^{-i0.292\pi}$
-70	$1.113e^{i0.664\pi}$	-0.195	$0.089e^{-i0.305\pi}$	$0.407e^{-i0.396\pi}$
-50	$0.941e^{i0.482\pi}$	-0.482	$0.158e^{-i0.181\pi}$	$0.478e^{-i0.487\pi}$
-30	$1.227e^{i0.249\pi}$	-0.879	$0.267e^{-i0.100\pi}$	$0.610e^{-i0.599\pi}$
-20	$1.583e^{i0.169\pi}$	-1.108	$0.323e^{-i0.069\pi}$	$0.732e^{-i0.653\pi}$
-10	$1.998e^{i0.118\pi}$	-1.330	$0.4363e^{-i0.035\pi}$	$0.905e^{-i0.692\pi}$

the interaction that breaks C_6 is much smaller than other terms. Hence C_6 will be a good approximate symmetry of the effective lattice model though it is not a microscopic symmetry.

Using these symmetries, the lattice tight-binding model can be written

$$H_K = -\sum_{\mathbf{x};\sigma}\sum_{m,n} t(m,n)\psi^\dagger_{+\sigma}(\mathbf{x}+m\mathbf{a_1}+n\mathbf{a_2})\psi_{+\sigma}(\mathbf{x}) + \text{H.c.} - \sum_{\mathbf{x};\sigma}\sum_{m,n} t^*(m,n)\psi^\dagger_{-\sigma}(\mathbf{x}+m\mathbf{a_1}+n\mathbf{a_2})\psi_{-\sigma}(\mathbf{x}) + \text{H.c.} \tag{5}$$

$\pm$ is valley index and $\sigma = \uparrow, \downarrow$ is spin index. We need only the following hopping terms: $t_1 = t(1,0)$, $t_2 = t(1,1)$, $t_3 = t(1,2)$, and $t_4 = t(2,0)$, and other terms that can be generated by C_6 rotation and M reflection symmetry.

We list tight binding parameters for different Δ_V in Table I and Fig. 2. A key feature [8] allowed by the symmetries is that within a single valley there is no time reversal, and hence there can be a nonzero flux through each triangular plaquette. However, this flux must be opposite on neighboring plaquettes. From the explicit calculations of the tight-binding parameters, we see that the staggered flux in one triangle for each valley is about 0.5π–2π in the regime $\Delta_V < -25$ meV. Such a valley contrasting flux strongly breaks the spin-valley

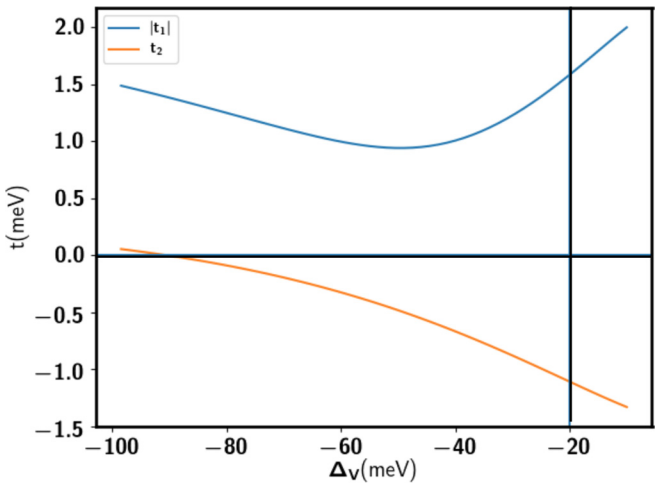

FIG. 2. Magnitude of the nearest neighbor hopping $|t_1|$ and the next-nearest-neighbor hopping t_2. t_2 has no imaginary part because of the Mirror reflection symmetry. The phase of t_1 is shown in Fig. 3. The vertical line labels $\Delta_V = -20$ meV where the bandwidth is equal to the Hubbard U: $W \approx U \approx 25$ meV.

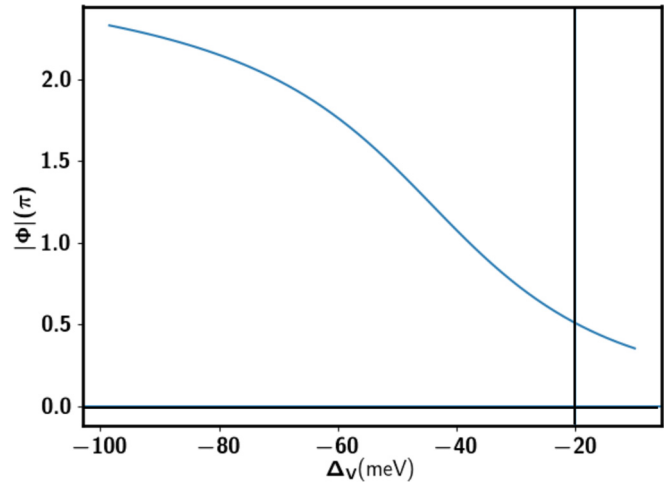

FIG. 3. The flux $|\Phi|$ of each triangle from the nearest neighbor hopping. For each triangle, two valleys experience opposite Φ. For each valley, Φ changes sign under C_6 rotation. The vertical line labels $\Delta_V = -20$ meV where the bandwidth is equal to the Hubbard U: $W \approx U \approx 25$ meV. For the Mott insulating regime at $\Delta_V < -25$ meV, we expect a large valley contrasting flux $|\Phi| \sim 0.5\pi - 2\pi$ trhough each triangle. Such a flux breaks SU(4) symmetry, which is inherited in the spin model for the Mott insulator through the superexchange term.

U(4) symmetry[2] down to $\text{U}(2)_+ \times \text{U}(2)_-$. Here, $\text{U}(2)_a$ means an independent SU(2) spin rotation combined with U(1) transformation for each valley a. As we show in the next section, this U(4) symmetry breaking term will be inherited in the spin-valley model of the Mott insulator through superexchange.

To obtain the interaction we start with the (screened) Coulomb interaction and project it on to the active valence bands, as explained in Appendix C. We find

$$H_V = \frac{U}{2}\sum_i n_i^2 + g_1 U \sum_{\langle ij\rangle} n_i n_j - \frac{2g_h U}{2}\sum_{\langle ij\rangle}\sum_{a_1 a_2;\sigma_1\sigma_2} \psi^\dagger_{i;a_1\sigma_1}\psi_{i;a_2\sigma_2}\psi^\dagger_{j;a_2\sigma_2}\psi_{j;a_1\sigma_1} + \frac{J'_H}{2}\sum_{\langle ij\rangle}\sum_{\sigma_1\sigma_2}\left(\psi^\dagger_{i;+\sigma_1}\psi_{i;-\sigma_2}\psi^\dagger_{j;-\sigma_2}\psi_{j;+\sigma_1} + \text{H.c.}\right) - J_H\sum_i\left(\frac{1}{4}n_{+i}n_{-i} + \mathbf{S}_{+\mathbf{i}}\cdot\mathbf{S}_{-\mathbf{i}}\right). \tag{6}$$

The first and second terms are the on-site and nearest-neighbor repulsions, respectively. The third term is an intersite Hund's interaction which preserves the U(4) symmetry (as do the first two terms). The last two terms however break U(4). The term proportional to J'_H is the U(4) symmetry breaking part of the nearest-neighbor Hund's coupling [it breaks U(4) down to $\text{U}(2)_+ \times \text{U}(2)_-$]. Finally the last term (proportional to J_H) is an on-site intervalley Hund's coupling

[2]This is a combination of total charge U(1) transformation and the spin-valley SU(4) rotation.

TABLE II. Parameters of interaction terms in units of meV for $\Delta_V = -30$ meV. To estimate these parameters, we use a screened Coulomb interaction $V(\mathbf{q}) = \frac{e^2}{2\xi_0\kappa}\frac{1}{q}(1 - e^{-qr_0})$ with $\kappa = 8$ and screening length $r_0 = 5a_M \approx 75$ nm. $g_1 \approx 0.4$ and $g_h \approx 0.008$ are estimated from Wannier orbital calculations explained in Appendix C. The dependence of the interaction parameters on Δ_V is weak.

U	g_1U	$2g_hU$	J'_H	J_H
25	10	0.4	0.05	0.136

term which breaks U(4) down to $U(1)_c \times U(1)_v \times SU(2)_s$ (up to modding by a discrete Z_2 group). Here $U(1)_c$ corresponds to the total charge conservation and $U(1)_v$ corresponds to the valley charge conservation. $SU(2)s$ is the spin rotation. In Table II, we list estimates of the parameters that enter the interaction Hamiltonian. We note that the dominant part of the interaction is given by the first three terms that preserve the U(4) symmetry. Thus, to leading order, we can only consider the SU(4) symmetric part in the interaction and view the Hund's coupling J'_H, J_H as small perturbations.

Equations (5) and (6) give the lattice model for $\Delta_V < 0$. The dominant terms correspond to a spin-valley extended Hubbard model on a triangular lattice. The most significant U(4) symmetry breaking is from the valley-contrasting flux in the hopping term. The interaction term is dominated by the on-site and nearest-neighbor Hubbard repulsion, which is guaranteed to be SU(4) symmetric. However, there is also a small ferromagnetic Hund's coupling term. Such a term plays an important role in the spin physics of the Mott insulator though its value is only 2% of the Hubbard U. The lattice model has an approximate $U(2)_+ \times U(2)_-$ symmetry, which is further broken down to $U(1)_c \times U(1)_v \times SU(2)_s$ by the on-site intervalley Hund's coupling J_H term.

The intersite Hund's coupling, like all the other interactions, emerge from projection of the Coulomb interaction. Why does the pure density-density interaction give rise, after projection, to such a Hund's interaction? The reason is that the microscopic density operator has a complicated form in terms of the lattice operators: $\rho^{\text{phy}}(\mathbf{x}) \sim c^\dagger_{i;a\sigma}c_{i;a\sigma} + a(c^\dagger_{i;+\sigma}c_{i;-\sigma}e^{-i2\mathbf{K}_o\cdot\mathbf{x_i}} + \text{H.c.}) + b_{ij}c^\dagger_{i;a\sigma}c_{j;a\sigma}$ with a, b_{ij} small but generically not zero. The a term gives the on-site intervalley Hund's coupling J_H and the b term gives the intersite Hund's coupling $2g_hU$ and J'_H terms. The a term originates from the fact that the intervalley bilinear $c^\dagger_+c_-$ gives an oscillating density wave with momentum $2\mathbf{K_o}$, where $\mathbf{K_o}$ is the large momentum in the original Brillouin zone of a pure graphene layer. The b term comes from the fact that two nearest-neighbor Wannier orbitals $\langle ij\rangle$ are not tightly confined and their electron densities overlap [8]. As is well-known the Wannier orbital is gauge dependent and a natural question to ask is if we can choose a good gauge to make these orbitals sufficiently tightly confined that $b \approx 0$. The answer is no: the reason is that local regions of the valence band have nonzero Berry curvature (though there is no net Chern number). Such a nonzero Berry curvature is lost in the above one-orbital lattice model. The cost of this loss is that the microscopic density operator can not be purely on-site. In momentum space, $\rho(\mathbf{q}) \sim \sum_{\mathbf{k}} \lambda_a(\mathbf{k},\mathbf{q})c^\dagger_{a;\mathbf{k}+\mathbf{q}}c_{a;\mathbf{k}}$. The form factor $\lambda_a(\mathbf{k},\mathbf{q}) \sim |F(\mathbf{k})|e^{i\mathbf{A}(\mathbf{k})\cdot\mathbf{q}}$ at small $\mathbf{q}$, where $\mathbf{A}(\mathbf{k})$ is the Berry connection. Due to the nonzero Berry curvature, the form factor $\lambda_a(\mathbf{k},\mathbf{q})$ can not be equal to 1 in any gauge. Thus the density operator can not be written as $\rho(\mathbf{q}) = \sum_{\mathbf{k}} c^\dagger_{a;\mathbf{k}+\mathbf{q}}c_{a;\mathbf{k}}$ in any gauge. As a consequence, in the lattice model (for any gauge choice), the microscopic density operator can not be pure on-site, and will include intersite hopping terms. The original pure density-density interaction will then lead to density-density, density-hopping, hopping-hopping interaction in the lattice models. As explained in the Appendix C, there are several terms generated, like correlated hopping and pair hopping terms. Of these the only term that does not involve double occupancy (which is suppressed by the Hubbard U) is the intersite Hund's coupling term $2g_hU$.

Response to magnetic field: valley Zeemann coupling

Not only does the one-orbital lattice model lose the information of the Berry curvature of the Bloch states, it also loses information on the orbital magnetic moment. It is well established that Bloch states have an orbital magnetic moment $m(\mathbf{k})$ in the z direction [17]. A large g factor for valley orbital magnetic moment has been proposed theoretically and verified experimentally in graphene systems [18–20]. A recent experiment sees evidence of a very large g factor(of the order of hundreds) for valley orbital magnetic moment in monolayer graphene/h-BN system [21]. Motivated by these previous results, we study the possibility of a large valley orbital magnetic moment in the TG/h-BN system within the continuum model.

The corresponding g factor $g(\mathbf{k}) = m(\mathbf{k})\frac{4m_e}{\hbar^2}$ is

$$g(\mathbf{k}) = -\frac{4m_e}{\hbar^2}Im\sum_{n'\neq n}\frac{\langle n|\partial_{k_x}H|n'\rangle\langle n'|\partial_{k_y}H|n\rangle}{\xi_n(\mathbf{k}) - \xi_{n'}(\mathbf{k})}, \quad (7)$$

where we suppressed the valley index $a = \pm$ in $H_a(\mathbf{k})$ and $|n_a(\mathbf{k})\rangle$. n is the valence band and $n' \neq n$ labels the other eigenstates of $H(\mathbf{k})$.

Time reversal guarantees that $g_+(\mathbf{k}) = -g_-(-\mathbf{k})$. An external out-of-plane magnetic field B couples linearly to this orbital moment:

$$H_B = -B\sum_{\mathbf{k}}(g_+(\mathbf{k})c^\dagger_+(\mathbf{k})c_+(\mathbf{k}) + g_-(\mathbf{k})c^\dagger_-(\mathbf{k})c_-(\mathbf{k})). \quad (8)$$

We calculated $g_a(\mathbf{k})$ following Eq. (7) within the continuum model. Generically $g_a(\mathbf{k})$ has a strong dependence on momentum $\mathbf{k}$. Its behavior for $\Delta_V < 0$ and $\Delta_V > 0$ are qualitatively different. The modified band structures that include this orbital magnetic field are presented in Appendix A.

For $\Delta_V < 0$, $g_+(\mathbf{k}) < 0$ and $g_-(\mathbf{k}) > 0$ for every $\mathbf{k}$. Therefore effectively we have a valley Zeeman coupling. The averaged g factor is $\bar{g} \approx 54$, much larger than the $g = 2$ for spin. Therefore for $\Delta_V < 0$, the most dominant effect of a small out-of-plane magnetic field is the splitting of valley energy, rather than the familiar spin Zeeman effect. In addition to the splitting of the average energy of the two valleys, the out-of-plane magnetic field also increases the bandwidth of one valley while reducing the bandwidth of the other valley, as shown in Fig. 4.

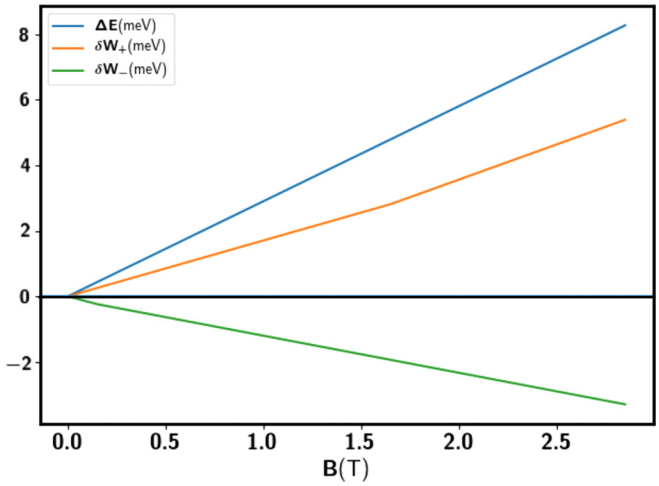

FIG. 4. Response to out of plane magnetic field B from the valley Zeeman coupling at $\Delta_V = -25$ meV. $\Delta E = \bar{E}_+ - \bar{E}_-$ is the splitting of the average energy of the valley $+$ and the valley $-$. δW_a is the change of the bandwidth for valley a. A small magnetic field $B = 1$ T split the average energy for two valleys by about 3 meV. Meanwhile the bandwidth of one valley is increased by around 1.5 meV while the bandwidth of the other valley is reduced by around 1.5 meV.

At small $B < 1$ T, this valley Zeeman coupling term can be used to polarize the valley in the Mott insulating regime. A larger $B \sim 3$ T can greatly increase the total bandwidth of the two valleys, which could destroy the Mott insulating phases. $B = 3$ T gives a flux per moiré unit cell $\Phi_B \approx 0.12\frac{h}{e}$. The system then crosses over to the Hofstadter butterfly region.

III. STRONG MOTT INSULATORS

We now discuss the experimentally observed insulating states [4] at filling $\nu_T = 1$ and $\nu_T = 2$ for $\Delta_V < 0$ using the model described in Sec. II. For the time being, we only focus on the strong-coupling limit $U \gg t$. In this case, charge is frozen and the low-energy physics is governed by an effective spin-valley model. At each site, we define the spin operator $\mathbf{S} = \frac{1}{2}c^\dagger_{a\sigma_1}\vec{\sigma}_{\sigma_1\sigma_2}c_{a\sigma_2}$ and the valley operator $\mathbf{I} = \frac{1}{2}c^\dagger_{a_1\sigma}\vec{\tau}_{a_1a_2}c_{a_2\sigma}$. Here, $\vec{\sigma}$ and $\vec{\tau}$ are Pauli matrices for the spin and the valley respectively.[3]

Using the standard t/U expansion (see Appendix E), we find the spin-valley model:

$$\begin{aligned} H_S = &\frac{J_1}{8}\sum_{\langle ij\rangle}(1+\tau_\mathbf{i}\cdot\tau_\mathbf{j})(1+\sigma_\mathbf{i}\cdot\sigma_\mathbf{j}) \\ &+ \frac{J_2}{8}\sum_{\langle\langle ij\rangle\rangle}(1+\tau_\mathbf{i}\cdot\tau_\mathbf{j})(1+\sigma_\mathbf{i}\cdot\sigma_\mathbf{j}) \\ &+ \frac{1}{8}\sum_{\langle ij\rangle}J^1_{p;ij}\left(\tau^x_i\tau^x_j+\tau^y_i\tau^y_j\right)(1+\sigma_\mathbf{i}\cdot\sigma_\mathbf{j}) \\ &+ \frac{1}{8}\sum_{\langle ij\rangle}J^2_{p;ij}\left(\tau^x_i\tau^y_j-\tau^y_i\tau^x_j\right)(1+\sigma_\mathbf{i}\cdot\sigma_\mathbf{j}) \\ &+ O\left(\frac{t^3}{U^2}\right), \end{aligned} \tag{9}$$

[3]We have assumed Einstein summation convention.

where $J_1 = -2g_hU + \frac{4t_1^2}{\tilde{U}}$ with $\tilde{U} = (1-g_1)U$ (=0.6U using the estimate in Table II) and $J_2 = \frac{4t_2^2}{U}$. J_1 has two contributions: a ferromagnetic part from the Hund's coupling and an antiferromagnetic part from the standard superexchange. Here $\tau^\mu_i\sigma^\nu_i$ should be understood as tensor product and is the abbreviation of the bilinear term $c^\dagger_{i;a_1\sigma_1}\tau^\mu_{a_1a_2}\sigma^\nu_{\sigma_1\sigma_2}c_{i;a_2\sigma_2}$. At $\nu_T = 1$, τ_i, and σ_i are simply the corresponding valley and spin operator. At $\nu_T = 2$, $\sum_{a\sigma}c^\dagger_{i;a\sigma}c_{i;a\sigma} = 2$ and the corresponding spin or valley operator at each site is a 4×4 matrix, which can be generated from the above bilinear terms of the fermionic operator. The factor $\frac{1}{8}$ is added to make the J consistent with the traditional convention in the spin $\frac{1}{2}$ model once valley is polarized.

$J^1_{p;ij}$ and $J^2_{p;ij}$ are the SU(4) symmetry breaking terms, mainly originating from superexchange term involving opposite valleys. The valley-contrasting phase in the hopping is inherited in this term. We have $J^1_{p;ij} = (J_1 + 2g_hU)(\cos 2\varphi_{ij} - 1) + J'_H$ and $J^2_{p;ij} = (J_1 + 2g_hU)\sin 2\varphi_{ij}$. The magnitude $|\varphi_{ij}| = \frac{|\Phi|}{3}$. Here φ_{ij} is the phase of the hopping for the valley $+$ of the bond $\langle ij\rangle$. $J'_H \approx 0.05$ meV is from the SU(4) breaking part of the Hund's coupling and can be neglected.

In the above, we ignore t_3 and t_4 for simplicity. One can easily add $J_3 = \frac{4t_3^2}{U}$ and $J_4 = \frac{4t_4^2}{U}$ terms. For the fourth neighbor coupling, the SU(4) breaking term from the valley-contrasting hopping phase should also be considered because t_4 has a large phase.

Even at second order of t/U expansion, we need to keep four parameters for the spin-valley model: J_1, J_2, Φ, and $2g_hU$. Ferromagnetic Hund's coupling $2g_hU \approx 0.4$ meV is even larger than J_1 and can not be ignored. These parameters can be tuned by Δ_V and a rich phase diagram may be accessible in the experiment. For $\Phi \sim 0.5\pi - 2\pi$, $J^1_{p;ij}$ and $J^2_{p;ij}$ are generically of the same order of J_1. Therefore the SU(4) symmetry is strongly broken to $\mathrm{SU}(2)_+ \times \mathrm{SU}(2)_- \times \mathrm{U}(1)_v$.[4] For $\nu_T = 2$, we also need to add the J_H term in Eq. (6) which further breaks down the symmetry to $\mathrm{U}(1)_v \times \mathrm{SU}(2)_s$.

A plot of $J_1 - J_2$ with Δ_V is shown in Fig. 5. J_1 can be tuned to be either ferromagnetic or antiferromagnetic. Though we have presented estimates of the parameters J_1, J_2, Φ, and $2g_hU$, their precise quantitative value are sensitive to assumptions used in the band structure calculation.[5] It is useful therefore to view them as phenomenological parameters and discuss the general phase diagram of the model in Eq. (9).

In the following two sections, we discuss the possible states for $J_1 < 0$ and $J_1 > 0$ region separately.

A. Ferromagnetic region

In the strict limit $\frac{t}{U} \to 0$, the Hund's coupling dominates over the other terms. Then $J_1 < 0$ and $J_2 \sim J^1_{p;ij} \sim J^2_{p;ij} \sim 0$. The Mott insulator should thus be a spin-valley ferromagnetic state.

[4]Strictly speaking, we need to further module some discrete symmetries.

[5]Even the sign of J_1 is sensitive to g_h. If g_h is increased by a factor of 2, J_1 will be ferromagnetic in the whole region of $U > W$.

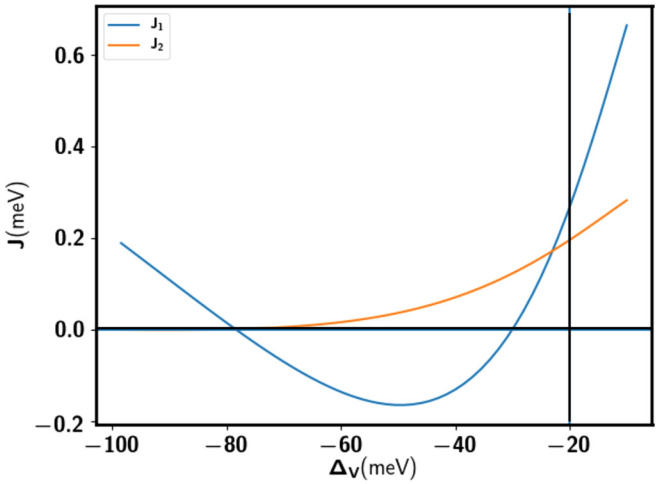

FIG. 5. $J_1 - J_2$ parameters with Δ_V. We fix $U = 25$ meV, $g_1 = 0.4$ and $g_h = 0.008$ in the calculation. The vertical line is the value of Δ_V for which the bandwidth $W = U$. Deep inside the Mott insulating phase, J_1 is ferromagnetic from the Hund's coupling. In the intermediate regime, both J_1 and J_2 are antiferromagnetic.

For $\nu_T = 1$, the ground state should be ferromagnetic. The spin is polarized to any direction because of the SO(3) spin rotation symmetry. For the valley, we need small anisotropic terms to decide whether τ_x or τ_z order is favored. The small SU(4)-breaking Hund's coupling J'_H ($\sim$0.05 meV) term in Eq. (6) favors τ_z valley polarization. But the anisotropy inherited from the valley-contrasting hopping term in $J^1_{p;ij}$ of in Eq. (9) favors the τ_x polarization. Therefore interaction term and kinetic term compete with each other. At the flat band limit, we always have the τ_z valley polarization. At any nonzero temperature T, the spin ferromagnetism will be disordered immediately because of the Mermin-Wagner theorem. However, valley polarization only breaks a discrete time-reversal symmetry and will therefore be stable upto a finite temperature continuous transition in the Ising universality class. The spontaneous breaking of time reversal at small nonzero T may give an exponentially suppressed but nonzero Hall conductivity. Such a valley polarization may also be detectable via the magneto-optical Kerr effect, as demonstrated in Ref. [22] for spin ferromagnetism. As the out-of-plane magnetic moment from the valley is 20 times larger than spin, this effect should be more significant for the valley polarized state. Once t/U is increased, there can be a phase transition to an inter-valley-coherent (IVC) order (τ_x polarization). The IVC order does not break the time-reversal symmetry. As it breaks the $U(1)_v$ symmetry, there can be a Berezinskii-Kosterlitz-Thouless transition (BKT transition) at finite temperature.

For $\nu_T = 2$, just from the $SU(2)_+ \times SU(2)_- \times U(1)_v$ symmetric interaction in Eq. (9) there are several degenerate states. The true ground state will be selected from these by small anisotropies. The onsite intervalley Hund's coupling J_H in Eq. (6) will select the spin polarized, valley singlet state as the ground state. Such a spin ferromagnetic state cannot have true long range order at any nonzero T.

In summary, for $\frac{t}{U} \to 0$ limit, the ground states for both $\nu_T = 1$ and $\nu_T = 2$ are ferromagnetic. There should be a finite temperature transition corresponding to the valley polarization for $\nu_T = 1$ and no transition for $\nu_T = 2$. We emphasize that the destruction of the spin ferromagnetism at finite temperature does not close the charge gap, which is at order U and is thus much larger than the ferromagnetic scale $J_1 \sim 0.01U$.

B. Antiferromagnetic region

With increasing t/U, we enter a regime dominated by the antiferromagnetic superexchange: $J_1, J_2 > 0$. The frustrated triangular geometry and the larger number of degrees of freedom[6] than the standard spin-1/2 model both enhance the effect of quantum fluctuations. Density matrix renormalization group (DMRG) calculations of Eq. (9) may be able to map the phase diagram. Here we restrict ourselves to brief comments about special cases where we can relate the model to others studied in the literature. At $\nu_T = 1$, because of of the large valley Zeeman effect, a small out of plane magnetic field (of order $\approx$0.2 T) can already give an energy splitting larger than J_1 and J_2. Then the valley is frozen into a polarized state, and the effective model becomes the standard Heisenberg $J_1 - J_2$ spin $\frac{1}{2}$ model. This model is already well studied [23–25]. At small J_2/J_1, the ground state is the well known 120° magnetically ordered state. At large J_2/J_1 ratio, the ground state is a stripe antiferromagnet. In the intermediate region, a spin liquid phase is suggested from DMRG calculations [23,24] though precisely which kind of spin liquid is not clear. Candidates are a chiral spin liquid or a U(1) Dirac spin liquid.

Another special case is to apply a large in-plane magnetic field to polarize the spin. We expect then that the remaining valley degree of freedom forms a 120° order at small J_2/J_1.

IV. WEAK MOTT INSULATORS: POSSIBILITY OF A CONTINUOUS MOTT TRANSITION

We now discuss the region close to the Mott metal-insulator transition for $\Delta_V < 0$. In this region, the spin-valley model derived in the previous section will not be adequate to discuss the Mott insulator. We could keep higher order terms in the t/U expansion which will include multisite ring exchange processes [26]. Alternately the physics (even in the insulating side) may be directly discussed within the framework of the original Hubbard model.

The Mott transition is of course most central to the study of correlated electron systems, and there is a vast literature [11]. It has long been appreciated that there are many distinct routes by which a metal may evolve into a Mott insulator at zero temperature. A common fate (realized in many experimental systems) is that the transition occurs between the paramagnetic metal and a magnetic insulator and is first order. Such a route can potentially be avoided in frustrated low-dimensional lattices (as pertinent to the present paper). A different route [27], suggested by a simple Hartree-Fock theory for an an-

[6]In the limit where we only keep $J_{1,2}$, we get an SU(4) antiferromagnet with spins in either the fundamental representation (at $\nu_T = 1$) or in the six-dimensional representation (at $\nu_T = 2$) of SU(4). Such models, even when nearest neighbor, are more likely to be in nonmagnetic ground states than their SU(2) versions.

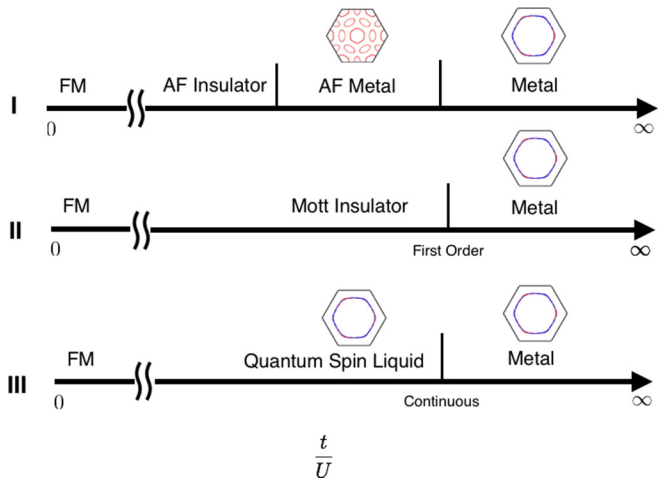

FIG. 6. Three possible phase diagrams tuned by t/U at $\nu_T = 2$. In (I), AF Metal means metal coexisting with antiferromagnetic order. AF insulator is a Mott insulator with antiferromagnetic order (The most likely candidate is the 120° valley order). In (II), the Mott insulator may be antiferromagnetic or may be a quantum spin liquid. In (III), the specific quantum spin liquid we consider has a spinon Fermi surface coupled to a U(1) gauge field. At $\frac{t}{U} = 0$, the ground state is a ferromagnet because of intersite Hund's coupling. We also show the plots of the Fermi surfaces. The Fermi surfaces are calculated at $\nu_T = 2$ using t_1, t_2, t_3, t_4 for $\Delta_V = -20$ meV. For the AF metal, we use the 120° intervalley order with the order parameter $M = 2|t_1|$. The Fermi surface area should decrease continuously in the AF metal region as $\frac{M}{|t_1|}$ increases.

tiferromagnetic order parameter,[7] is that the paramagnetic metal first undergoes a magnetic ordering transition into a magnetic metal. Eventually there is a second transition where the magnetic metal becomes a magnetic insulatior. A third fascinating alternative is that there is a continuous quantum critical Mott transition. A theory for such a continuous Mott transition [12] exists when the Mott insulator is a quantum spin liquid with a neutral spinon Fermi surface coupled to a U(1) gauge field. Such a continuous Mott transition may be relevant to experiments [28,29] on quasi-two-dimensional organics. It is currently not at all clear if other kinds of Mott insulators admit continuous zero-temperature quantum phase transitions into the paramagnetic metal. The three possible evolutions discussed above from metal to Mott insulator are illustrated in Fig. 6.

The TG/h-BN (and other graphene moiré systems) offers a tremendous opportunity to explore the band-width controlled Mott transition in a frustrated two-dimensional lattice. There is a large body of very interesting prior work (see, for instance, Refs. [28–32]) on quasi-two-dimensional organic salts (also on triangular lattices) which has probed the Mott transition with pressure as a tuning parameter at low temperature. Compared to the organics, the graphene system has the advantage that the electric control of bandwidth should make it a lot easier to tune through the Mott transition at low temperature and study it in exquisite detail.

With this in mind below we propose concrete (and we believe, feasible, in TG/h-BN) experiments that distinguish these various routes to the Mott transition.

A. "Magnetic" metal as an intermediate phase

We first consider the situation where the evolution from the metal to an antiferromagnetic (in spin-valley space) Mott insulator occurs in two stages. First there is a phase transition inside the metallic phase where the entiferromagnetic order onsets leading to a modification of the unit cell. This reconstructs the Fermi surface. With increasing amplitude of the antiferromagnetic order parameter, the Fermi surfaces will shrink and there will be a further transition to an antiferromagnetic insulator. This is the natural result of a Hartree-Fock treatment of the interactions. In the TG/h-BN context, such a symmetry breaking is suggested to arise from the nesting of the Fermi surfaces for $\nu_T = 2$ by Ref. [10]. Nesting driven theories have also been proposed for the twisted bilayer graphene system [33,34].

A clear experimental probe of this scenario is to study Shubnikov-DeHaas (SdH) oscillations in the resistivity in a perpendicular magnetic field. Through out the paramagnetic metal phase the Fermi surface area, and hence the SdH frequency, is fixed to be a constant by Luttinger's theorem. In the antiferromagnetic metal, the reconstruction of the Fermi surface will change the SdH frequencies. On approaching the insulator these frequencies will decrease (possibly all the way to zero if the transition from the antiferromagnetic metal to antiferromagnetic insulator is continuous). Thus in this scenario there will be a change in the SdH frequencies *before* the metal becomes an insulator similar to Fig. 7. We caution that the SdH experiments should be performed in *low* perpendicular magnetic field so that they are a soft probe of the Fermi surface of the metal. At larger fields, we will enter the quantum Hall regime and the oscillations may not directly reveal the Fermi surface structure of the zero field metal.

Let us briefly further comment on this simple Hartree-Fock scenario. In the strong Mott insulating region, the system may possibly be in a spin-valley ordered antiferromagnetic phase. However the mechanism for such ordering is different in the metal where it may be driven by an approximate nesting of the Fermi surface. Reference [10] suggested such a nesting driven mechanism for $\nu_T = 2$ by using a nearest-neighbor tight binding model with valley contrasting flux $\Phi = \frac{\pi}{2}$. However, according to our calculation in Fig. 3, the flux Φ is generically not equal to $\frac{\pi}{2}$ and t_2, t_3, t_4 are also necessary to reproduce the band structures. One natural question is whether this nesting of Fermi surfaces at $\nu_T = 2$ is fine tuned or not. To test the robustness of the nesting properties of the Fermi surfaces, we calculated the Density of States(DoS) at $\Delta_V = -5, -10, -15, -20, -25, -30$, and -40 meV using the continuum model with a 300×300 mesh-grid in momentum space. The Van-Hove singularity in our model is away from the Fermi level at both $\nu_T = 1$ and $\nu_T = 2$ as shown in Fig. 8. From the Fermi surface plots in Appendix A, one can also see that there is no nesting instability in the particle-hole channel. Thus it is not obvious that the Hartree-

[7] In the following, we will use the term "magnetic" to denote ordering in the spin-valley space.

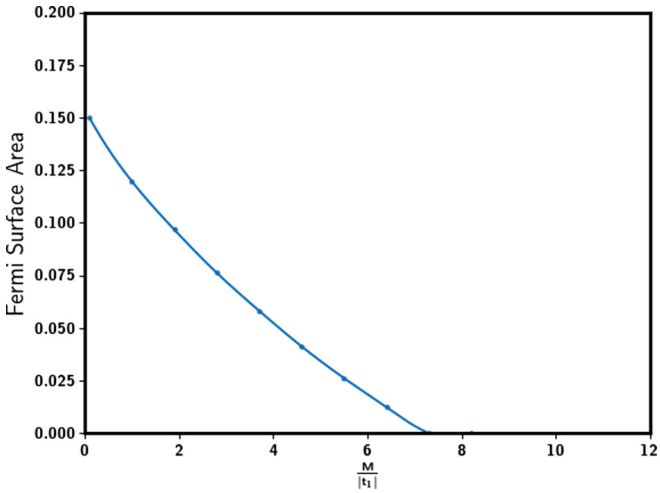

FIG. 7. The change of Fermi surface area(in units of the area of the MBZ) with order parameter M for the 120° intervalley order: $H_M = -M \sum_{\mathbf{x}} c^\dagger_{\mathbf{x}}(\cos(\mathbf{Q}\cdot\mathbf{x})\tau_x + \sin(\mathbf{Q}\cdot\mathbf{x})\tau_y)c_{\mathbf{x}}$ with $\mathbf{Q} = (\frac{4\pi}{3}, 0)$. We use $t_1 = 2.14e^{i0.141\pi}$ meV and $t_2 = -1.372$ meV for $\Delta_V = -20$ meV. There are several Fermi surfaces and we only count the hole pocket at Γ point. At $M \to 0$, magnetic breakdown effect should give a quantum oscillation frequency corresponding to the original Fermi surface area equal to 0.5, which is not captured by our calculation here. After adding a nonzero t_2, Fermi surfaces can not be fully gapped out until $M = 8|t_1|$.

Fock scenario is realized in the experimental system. We will therefore consider also other scenarios for the evolution from metal to insulator.

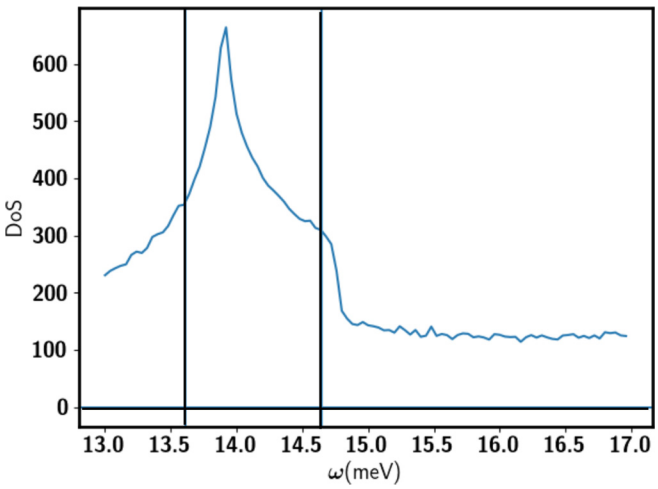

FIG. 8. Density of state at $\Delta_V = -25$ meV. Two vertical lines correspond to $\nu_T = 1$ and $\nu_T = 2$. The Van Hove singularity is away from both $\nu_T = 1$ and $\nu_T = 2$. This is true for other values of D in the region $-40 < \Delta_V < -5$ meV. The closest distance to $\nu_T = 1$ for the Van-Hove singularity is still at least 10% doping away. The Van-Hove singularity is associated with a Lifshitz transition of the Fermi surfaces (see Appendix A). At exactly $\nu_T = 1$ and 2, there is no obvious instability for the Fermi surfaces.

B. First-order Mott transition

A common possibility is that there is a first-order transition between the paramagnetic metal and a Mott insulator. This may happen irrespective of the detailed description of the insulator (antiferromagnetic or quantum spin liquid). In this scenario, the Fermi surface area seen in quantum oscillations should be constant in the metallic region. The first-order transition will be accompanied by hysteresis when D is cycled through the metal-insulator transition.

Further a $T = 0$ first-order transition will continue to $T \neq 0$ (till a critical end-point in the Ising universality class) as a sharp transition. Hysteresis will be observed on crossing this finite T phase boundary. If such a first-order transition is indeed seen the shape of the transition line in the T-D plane may provide some clues[8] about the nature of the Mott insulator.

C. Bandwidth controlled continuous metal-insulator transition

It is hard to theoretically rule out either of the two scenarios described above. However, for the simpler problem of the spin-1/2 triangular lattice Hubbard model, it seems (from numerical studies [26,35–38]) that a quantum spin liquid state forms in the weak Mott insulating regime. Many existing numerical calculations [26,35–37] as well as experiments [30,32] on the organics are broadly consistent with this being a spin liquid with a neutral Fermi surface. A recent DMRG calculation [38] however reports instead a gapped chiral spin liquid in the weak Mott region. The TG/h-BN system has more degrees of freedom (than the spin-1/2 Hubbard model) at each site which may make a spin liquid more likely in this regime.

A remarkable feature of the neutral Fermi surface state is that it admits a continuous Mott transition to the metal. We turn therefore to how to look for this experimentally.

We first review a (small generalization of a) theory [12] for the continuous Mott transition between a Fermi liquid metal and a spin liquid Mott insulator with a spinon Fermi surface coupled to a U(1) gauge field. The theory should work for both $\nu_T = 1$ and $\nu_T = 2$. We use the slave boson construction [39]: write $\psi_{a\sigma}(\mathbf{x}) = b(\mathbf{x})f_{a\sigma}(\mathbf{x})$. Here, $b(\mathbf{x})$ is a boson that carries the electric charge of the electron but not its spin/valley quantum numbers and $f_{a\sigma}(\mathbf{x})$ (the spinon) is an electrically neutral fermion that carries the spin/valley quantum number. There is a constraint $n_b = n_f = n_\psi$ relating the number of b, f and ψ particles at each site of the lattice. Correspondingly there is a U(1) gauge redundancy $b(\mathbf{x}) \to b(\mathbf{x})e^{i\alpha(\mathbf{x})}$ and $f_{a\sigma} \to f_{a\sigma}e^{-i\alpha(\mathbf{x})}$. A reformulation of the original electronic problem in terms of the (b, f) variables necessarily must include a dynamical U(1) gauge field. In the Fermi liquid phase the spinons form a Fermi surface while

[8]Specifically, through the Claussius-Clapeyron relation, the metal-insulator phase boundary will tilt toward the insulator or metal depending on which state has more entropy at a given low T. An antiferromagnetic insulator will at low-T have lower entropy than the metal while some spin liquid insulators have higher entropy than a metal.

$\langle b \rangle \neq 0$, i.e., the bosons are in a superfluid state. Upon increasing interactions, a Mott insulator will form. Within this slave particle framework a natural Mott insulator is obtained by letting b form a bosonic Mott insulator (where $\langle b \rangle = 0$ while keeping the f-Fermi surface [40]. The resulting state is a spin liquid Mott insulator. The Mott metal-insulator transition is then associated [12,39,41] with the superfluid-Mott transition of the boson b in the presence of the spinon Fermi surface and the U(1) gauge field. As shown in Ref. [12] the resulting theory admits a continuous Mott transition which further is tractable. We now highlight two predictions of this theory for transport experiments that may be directly feasible in TG/h-BN.

The first pertinent prediction is a universal jump [12,42] by $R\frac{\hbar}{e^2}$ of the residual resistivity as the Mott critical point is approached from the metallic side.[9] Here, R is a universal number of O(1). At a nonzero temperature, the resistivity follows a useful scaling form described in Ref. [42]:

$$\rho(T,\delta) - \rho_m = \frac{\hbar}{e^2} G\left(\frac{\delta^{z\nu}}{T}\right) \tag{10}$$

with $z = 1$, and $\nu \approx 0.672$ in a clean sample. ρ_m is the residual resistivity in the metal just before the Mott transition and δ is the parameter used to tune across the transition. For TG/h-BN, this is accomplished very simply by the perpendicular displacement field. Thus the TG/h-BN system offers a promising platform to access such a continuous Mott transition.

A second prediction enables directly detecting the neutral Fermi surface, if it exists, just on the insulating side of the Mott transition: such a neutral Fermi surface will lead to SdH oscillations [43–45] in a weak Mott insulator. Detailed expressions for the temperature dependence of such oscillations may be found in Ref. [45]. The key point is that though the spinons are electrically neutral, they couple to the internal U(1) gauge field $\mathbf{a}$, which locks to an external field $\mathbf{A}$: $\mathbf{a} = \alpha\mathbf{A}$ with a factor $\alpha < 1$. In the vicinity of Mott transition point, α will be of order 1. Therefore the spinon Fermi surface experiences an internal magnetic field $\mathbf{b} = \alpha\mathbf{B}$ and show quantum oscillation in the resistivity ρ_f. At finite temperature, ρ_b is large but finite even inside the Mott insulator, and therefore $\rho = \rho_b + \rho_f$ should also show quantum oscillation with frequency enlarged by a factor of $\frac{1}{\alpha}$ compared to the Fermi liquid side. α should show dependence on voltage D and also temperature (see Ref. [45]). Due to the large valley Zeeman coupling, in practice, the oscillations may not have perfect periodicity in $1/B$. However, an oscillating response to B inside a Mott insulator will be strong evidence of the existence of neutral Fermi surface and emergent gauge field. Remarkably SdH oscillations in electrical resistivity have been reported in a recent experiment on a mixed valence insulator [46].

[9]A simple explanation is from the Ioffe-Larkin rule which states that the physical resistivity $\rho = \rho_b + \rho_f$, where $\rho_{b,f}$ are the boson and f-fermion resistivities, respectively. Across the Mott transition, ρ_f evolves smoothly while ρ_b goes from 0 (in the metal) to a universal constant $= R\frac{\hbar}{e^2}$ (at the critical point) and eventually is ∞ (in the insulator). The universal resistivity jump follows.

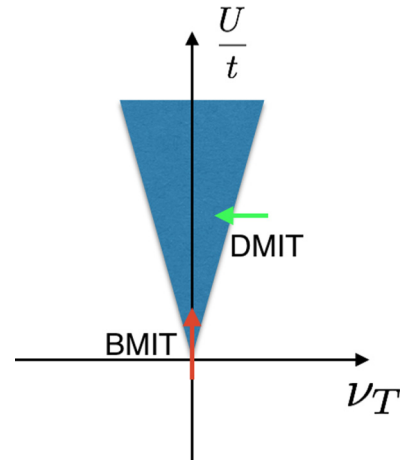

FIG. 9. Illustration of bandwidth-controlled metal-insulator transition (BMIT) and doping-controlled metal-insulator transition (DMIT). The shaded region is the Mott insulator.

Another more direct evidence for a spinon Fermi surface state is metallic thermal transport $\sigma_{\text{thermal}} \sim T$. Measurement of the thermal conductivity is hard, but may be possible in the future.

We emphasize that the only currently understood theory for such a continuous Mott transition is when the insulator is a U(1) spin liquid with an emergent neutral Fermi surface [12]. It is not known if there could be a direct continuous Mott transition between the paramagnetic metal and other kinds of Mott insulators (for instance, an antiferromagnetic insulator or a chiral spin liquid). Such a continuous transition is exotic and will presumably involve a novel formulation. In TG/h-BN if none of the signatures discussed above are seen it will provide experimental evidence for such an exotic continuous quantum phase transition.

D. Doping controlled continuous metal-insulator transition

We now briefly address the Mott metal-insulator transition induced by doping away from commensurate filling. We will restrict to a discussion of the possibility of a continuous Mott transition,[10] which is possible if the Mott insulator is in the quantum spin liquid with a spinon Fermi surface. Theoretical descriptions of this doping-controlled metal-insulator transition (DMIT) may be found in Refs. [12,47,48], see Fig. 9. Similar to our description of the bandwidth-controlled metal-insulator transition (BMIT) in the previous section, we still use the slave boson theory: $c = bf$. In this case, boson b goes through a chemical potential tuned superfluid-Mott insulator transition. We focus here on the predictions for electrical transport. From the Ioffe-Larkin rule $\rho_c = \rho_b + \rho_f$. In the clean limit at a small but nonzero T it is known [48] that the bosons have a resistivity $\rho_b \sim \frac{1}{\log_{10}\frac{1}{T}}$ due to scattering from (Landau-damped) gauge fluctuations. The weak logarithmic

[10]Strictly speaking continuous Mott transitions are also possible out of paired spin liquid states. For instance, if we dope a Z_2 spin liquid, a natural outcome is a superconductor. We then have a continuous Mott insulator-superconductor transition.

dependence may not be visible, and hence we may roughly expect the residual resistivity to jump as the critical point is approached from the metallic side just like at the BMIT.

Disorder effects will further affect the nature of the transition. First it is natural that at very low densities the dopants will be localized. The DMIT will then happen at a nonzero critical doping. The bosons are expected to have a universal conductivity at this disordered critical point which is distinct from that in the BMIT case. Thus, close to the critical point, we will once again have a universal jump of residual resistivity. Finally we note that near the disordered critical point, scaling similar to Eq. (10) will hold but with different values for the exponents z and ν. From the general result $\nu \geqslant \frac{2}{d} = 1$(where $d = 2$ is the spatial dimension) for disordered critical points, and the expectation $z = 1$ in the presence of Coulomb interactions, we have $z\nu \geqslant 1$ for the DMIT, larger than $z\nu \approx 0.672$ for the BMIT of a clean system.

This brief discussion was meant to motivate an experimental study of the doping induced Mott transition in TG/h-BN. Interestingly the existing experimental data may already have evidence for a continuous doping controlled metal-insulator transition (DMIT) close to $\nu_T = 2$. In the Fig. 3(a) of Ref. [4], there is a critical $V_t^c \approx -4.7$ V for V_t which controls the total density (and also the bandwidth). Resistance R increases with temperature T when $V_t < V_t^c$ while when $V_t > V_t^c$ the resistance R decreases with T. At exactly V_t^c, the resistance is finite (around $0.7\frac{h}{e^2}$) and constant in the temperature region 1.5–40 K. Here 1.5 K is the lowest temperature reachable in the reported experiment in Ref. [4]. This suggests a continuous metal-insulator transition. As a further test, we suggest measurements at lower temperature and to scale the data according to Eq. (10) but with modified exponents as discussed above. It is also interesting to study the temperature dependence of the resistivity close to the critical point to search for non-Fermi-liquid behavior.

Finally within the theory of Ref. [12] the quasiparticle effective mass in the metallic phase will diverge as $\frac{1}{\sqrt{\delta}}$ (up to logarithmic corrections) where δ is the doping away from the Mott insulator. This strong divergence may be observable through SdH measurements. (In contrast at the BMIT, a much weaker logarithmic divergence of the effective mass is predicted).

V. COMMENTS FOR THE $\Delta_V > 0$ SIDE

When $\Delta_V > 0$, the valence bands of two valleys have nonzero Chern numbers $C = \pm 3$. Therefore it is not possible to construct localized Wannier orbitals for each valley separately. Following a similar construction [8] for twisted bilayer graphene, we can construct a two orbital model on the triangular lattice (see Appendix D) but with a non-on-site implementation of the valley charge operator (i.e., the valley charge operator is not a sum of on-site terms). As a consequence, the interaction is in a complicated form, which makes an analytical treatment of the model very hard. Such a model may be useful for future numerical simulations.

Despite the complexity of the model, the $\Delta_V > 0$ side can potentially realize interesting phases that show the quantum anomalous Hall effect (QAHE) and even the fractional quantum anomalous Hall effect (FQAHE) as proposed in our previous paper [6]. Especially, similar to quantum Hall ferromagnets, the $\nu_T = 1$ insulator in the flat band limit should be a spin and valley polarized Chern insulator with Hall conductivity $\sigma_{xy} = 3\frac{e^2}{h}$ even at zero magnetic field. One concern about the experimental realization of this QAHE state is that the energies of the two valley polarizations are degenerate at zero magnetic field and hence the system forms domains. However one can align the valley polarization by cooling in an out-of-plane magnetic field. As shown in Fig. 10, there is also a valley Zeeman coupling when $\Delta_V > 0$. The averaged g factor is not so large as the $\Delta_V < 0$ side because $g(\mathbf{k})$ changes sign in the MBZ. However, within our model, for a z direction magnetic field with 1 T, the bandwidth of one valley becomes 6 meV smaller than the other valley. Therefore one valley polarization should be selected by a magnetic field and the system will be in the QAHE state. The total filling of the QAH insulator should also change with the magnetic field, leading to an insulating Landau fan: $\nu_T = 1 - 3|\Phi_U|$ where Φ_U is the uniform flux per moiré unit cell in units of h/e. For zero twist angle, $|\Phi_U| \approx 0.04$ for $B = 1$ T.

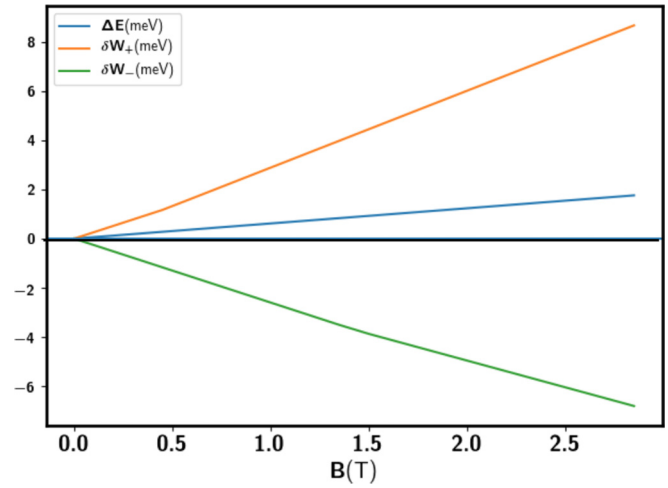

FIG. 10. Response to out of plane magnetic field B from the valley Zeeman coupling at $\Delta_V = 25$ meV. $\Delta E = \bar{E}_+ - \bar{E}_-$ is the splitting of the average energy of the valley $+$ and the valley $-$. δW_a is the change of the bandwidth for valley a.

The proposal of quantum Hall ferromagnetism in our previous paper [6] assumes the flat band limit $\frac{W}{V} \to 0$. The possible phases at intermediate W/V remain an open question, as does the nature of the evolution from the weak interacting metal. A simple possibility is that there is a an intermediate ferromagnetic metallic phase which then gives way to the ferromagnetic insulator. Clarifying this will require developing tools to deal with strong correlations in partially filled dispersing $\pm$ Chern bands which we leave for the future.

VI. CONCLUSION

In this paper, we discussed several aspects of the moiré superlattice system in ABC stacked trilayer graphene on hexagonal boron nitride where previous work has shown that an applied vertical electric field D can tune both the bandwidth and the topology. Our focus in this paper was complementary to our earlier work which mainly discussed the phenomenol-

ogy of the topologically nontrivial side ($\Delta_V > 0$). Here we mainly discussed the other topologically trivial side($\Delta_V < 0$). We explicitly constructed a lattice extended Hubbard model with SU(4) degrees of freedom [but no SU(4) symmetry]. We used this model as a framework to discuss possible Mott insulating states at at total filling $\nu_T = 1$ and $\nu_T = 2$. We also showed that due to a large valley Zeeman coupling a small perpendicular magnetic field may be a useful knob in this system.

We emphasized the opportunities provided by TG/h-BN (and other graphene moiré structures) to carefully experimentally study the bandwidth tuned Mott metal-insulator transition in a frustrated two-dimensional lattice. We showed how simple electrical transport experiments can distinguish many different routes to the Mott transition. Particularly exciting is the possibility that this system realizes a quantum spin liquid with a spinon Fermi surface in the vicinity of the Mott transition. Such a state admits a direct continuous Mott transition to the Fermi liquid metal. The transport experiments we describe can specifically also probe this state and the continuous Mott transition.

Finally when $\Delta_V > 0$ and the bands have Chern number $C = \pm 3$, we constructed a lattice two orbital model on the triangular lattice but with a nonlocal implementation of the valley charge operator (along the lines of the treatment of twisted bilayer graphene in Ref. [8]). It remains to be seen whether this kind of model can be useful for a future attack on strongly correlated partially filled $\pm$ Chern bands.

ACKNOWLEDGMENTS

We thank Yuan Cao, Debanjan Chowdhury, Mao Dan, Pablo Jarillo-Herrero, Adrian Po, Cecile Repellin, Ashvin Vishwanath, Feng Wang, Liujun Zou, and Mike Zaletel for many inspiring discussions. This work was supported by NSF grant DMR-1608505, and partially through a Simons Investigator Award from the Simons Foundation to Senthil Todadri.

APPENDIX A: BAND STRUCTURES

First we give a brief introduction to the continuum model approach used in Ref. [6] and the current paper. If the two layers have slightly different lattice constants a_1 and a_2, or a small twiste angle θ, then there is a moiré super lattice with lattice constant $a_M \approx \frac{a}{\sqrt{\xi^2+\theta^2}}$ where $\xi = \frac{|a_1-a_2|}{a_2}$. For TG/h-BN system, even if the twist angle $\theta = 0$, there is still a moiré superlattice with $a_M \approx 58$ a, where $a \approx 0.246$ nm is the lattice constant for the graphene layer. Besides, we treat the two valleys separately. The two valleys are related by time-reversal transformation. Therefore we can do calculations for only one valley, for example, valley $+$.

First we ignore the h-BN layer. Then the ABC stacked trilayer graphene has cubic band touching at two momentum points K_o and K_o' in the original Brillouin zone (BZ). We label the two valleys as $+$ and $-$. For each valley, the effective low-energy model is a simple two band model, consisting of the A sublattice of the top graphene layer and the B sublattice of the bottom graphene layer. Other degrees of freedom are not active at low energy, and can be ignored. For the valley $+$, the effective model in the basis (c_A^t, c_B^b) is

$$h_+(\mathbf{k}) = \begin{pmatrix} \frac{\Delta_V}{2} & \frac{t^3}{\gamma_1^2}(k_x - ik_y)^3 + 2\frac{t\gamma_3}{\gamma_1}|\mathbf{k}|^2 \\ \frac{t^3}{\gamma_1^2}(k_x + ik_y)^3 + 2\frac{t\gamma_3}{\gamma_1}|\mathbf{k}|^2 & -\frac{\Delta_V}{2} \end{pmatrix}. \tag{A1}$$

We use $t = -3000\frac{\sqrt{3}}{2}$ meV, $\gamma_1 = 380$ meV, and $\gamma_3 = 293\frac{\sqrt{3}}{2}$ meV. γ_1 and γ_3 are interlayer hoppings [49]. However we do not expect these parameters to be quantitatively precise. In the above equation, momentum $\mathbf{k}$ is in units of $1/a$. Δ_V is the energy difference between the top and the bottom graphene layers, which is controlled by an applied voltage. The model for the valley—is the time-reversal transformation of the above model.

Then moiré lattice gives a superlattice potentials:

$$H_M = \sum_{a;\mathbf{k},\mathbf{G_j}} c_{a;t}^\dagger(\mathbf{k}+\mathbf{G_j})V(\mathbf{G}_j)c_{a;t}(\mathbf{k}) + \text{H.c.}, \tag{A2}$$

where G_j is the moiré superlattice reciprocal vector and $a = +, -$ is the valley index. We choose $\mathbf{G_1} = (0, \frac{4\pi}{\sqrt{3}a_M})$ and $\mathbf{G_2} = (-\frac{2\pi}{\sqrt{3}a_M}, \frac{2\pi}{a_M})$ for the moiré Brillouin zone (MBZ). Because only the h-BN on top of the graphene is aligned and effective, we expect the moiré superlattice potential only acts on the c_A^t component. We use $V(\mathbf{G_1}) = V_0 e^{i\theta_0}$ with $V_0 = -14.88$ meV and $\theta_0 = -50.19°$. $V(G_j)$ for other j can be generated by C_6 rotation: $V(C_6 G) = V(G)^*$. The bandwidth can be tuned by Δ_V, as shown in Fig. 11.

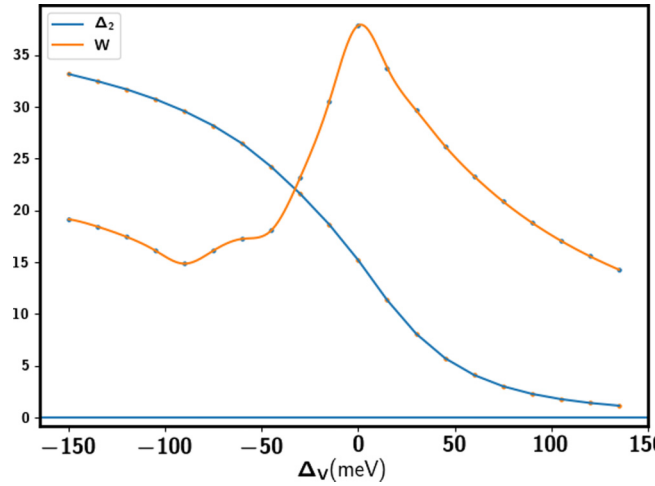

FIG. 11. The dependence of the bandwidth W and the band gap Δ_2 on the applied vertical voltage difference D. Δ_2 is the minimal gap between the valence band and the band below. W and Δ_2 are all in units of meV. The band gap Δ_1 between the conduction band and the valence band is almost equal to $|\Delta_V|$ and becomes larger than the bandwidth after $|\Delta_V| > 30$ meV.

1. Symmetry

We first discuss the symmetries of the continuum model of Eqs. (A1) and (A2).

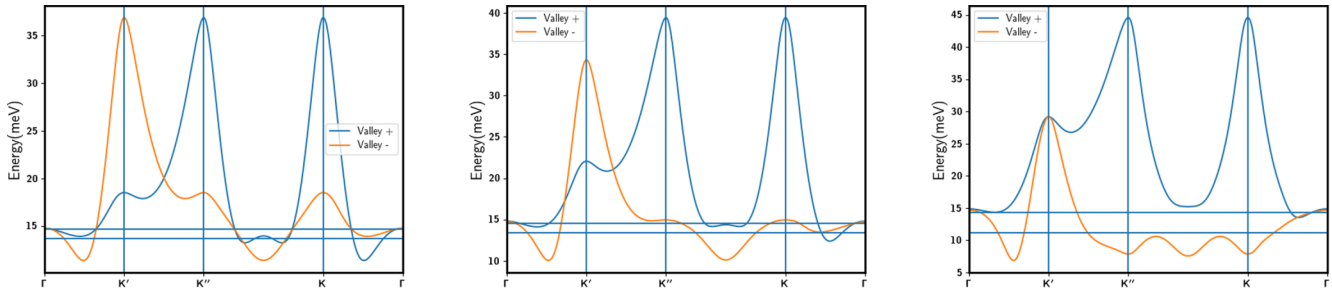

(a) $\Delta_V = -25$ meV, $B = 0$ T, $C = 0$ (b) $\Delta_V = -25$ meV, $B = 1$ T, $C = 0$ (c) $\Delta_V = -25$ meV, $B = 3$T, $C = 0$

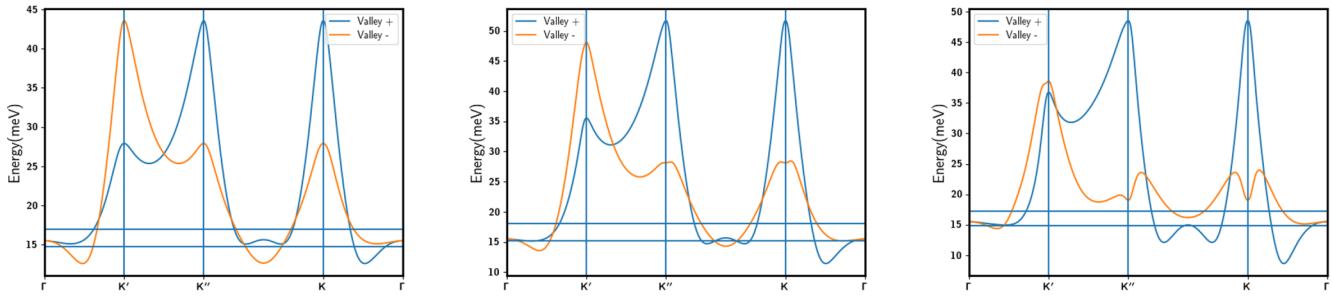

(d) $\Delta_V = 25$ meV, $B = 0$ T, $C = \pm 3$ (e) $\Delta_V = 25$ meV, $B = 1$ T, $C = \pm 3$ (f) $\Delta_V = 25$ meV, $B = 3$T, $C = \pm 3$

FIG. 12. Band structures of the valence bands in the hole picture for $\Delta_V = -25$ and 25 meV in ab out-of-plane magnetic field B. $K' = (0, \frac{4\pi}{3a_M})$. $K'' = (\frac{2\pi}{\sqrt{3}a_M}, \frac{2\pi}{3a_M})$, and $K = (0, -\frac{4\pi}{3a_M})$ are equivalent in the MBZ. Two horizontal lines are the chemical potential for $\nu_T = 1$ and $\nu_T = 2$. For $\Delta_V < 0$, out-of-plane magnetic field split the energies of two valleys. It also increases the bandwidth of one valley while reducing the bandwidth of the other valley. For $\Delta_V > 0$, out-of-plane magnetic field increase the bandwidth of one valley while decrease the bandwidth of the other valley.

First, there is time-reversal symmetry which relates the two valleys: complex conjugation combined with $c_{+,\alpha}(\mathbf{k}) \to c_{-,\alpha}(\mathbf{k})$ where $\alpha = t, b$ is the spinor index. Both Eqs. (A1) and (A2) are also apparently invariant under C_3 rotation symmetry: $c_{a;\alpha}(\mathbf{k}) \to c_{a;\alpha}(C_3\mathbf{k})$ where $a = +, -$ is the valley index and $\alpha = t, b$ is spinor index in Eq. (A1). There is no inversion symmetry (and therefore C_6 rotation symmetry) in Eqs. (A1) and (A2).

Within the continuum model there is also a mirror reflection symmetry along the $\mathbf{G_6} = (2\pi, \frac{2\pi}{\sqrt{3}})$: $\theta(M\mathbf{k}) = \frac{\pi}{3} - \theta(\mathbf{k})$ where $\theta(\mathbf{k})$ is the angle of $\mathbf{k}$ in the polar coordinate. The Hamiltonian in Eqs. (A1) and (A2) is invariant under the mirror symmetry $c_{+,\alpha}(\mathbf{k}) \to c_{-;\alpha}(M\mathbf{k})$. However, microscopically this mirror reflection should be broken by the h-BN layer. We view it as a a good approximation in the continuum model.

2. Band structures in a small out-of-plane magnetic field

The moiré superlattice folds the orginal band of TLG to an MBZ, which is a hexagon. We take both valleys of the original band to be the Γ point of the MBZ.

We show band structures of the valence bands for TLG/h-BN system in a small out-of-plane magnetic field in Fig. 12 incorporating the effects of the valley Zeeman coupling.

3. Fermi surfaces at $\nu_T = 1$ and 2 for $\Delta_V < 0$

To aid the discussion of the metal-insulator transition for $\nu_T = 1$ and 2 in the $\Delta_V < 0$ side, we provide the plots of the Fermi surfaces at several different values of Δ_V in Fig. 13. In our model, the Fermi surfaces do not have an obvious nesting instability in the particle-hole channel. For $\nu_T = 1$, the filled Fermi sea has the topology close to $\Delta_V \approx -20$ meV.

APPENDIX B: HAMILTONIAN IN MOMENTUM SPACE

In momentum space, we focus on the four valence bands labeled by spin $\sigma = \uparrow, \downarrow$ and valley $a = +, -$. The density operator projected to the valence bands is

$$\rho(\mathbf{x}) = \sum_{a\sigma,\mathbf{k},\mathbf{q}} \lambda_a(\mathbf{k},\mathbf{q}) c^\dagger_{a\sigma}(\mathbf{k}+\mathbf{q}) c_{a\sigma}(\mathbf{k}) e^{-i\mathbf{q}\cdot\mathbf{x}} + \sum_{\sigma,\mathbf{k},\mathbf{q}} (\lambda_{+-}(\mathbf{k},\mathbf{q}) c^\dagger_{+\sigma}(\mathbf{k}+\mathbf{q}) c_{-\sigma}(\mathbf{k}) e^{-i(2\mathbf{K}+\mathbf{q})\cdot\mathbf{x}}$$
$$+ \lambda_{-+}(\mathbf{k},\mathbf{q}) c^\dagger_{-\sigma}(\mathbf{k}+\mathbf{q}) c_{+\sigma}(\mathbf{k}) e^{-i(-2\mathbf{K}+\mathbf{q})\cdot\mathbf{x}}), \tag{B1}$$

where $\mathbf{K} = (\frac{4\pi}{3a}, 0)$, $a = 0.236$ nm is the lattice constant of the graphene layer. Form factors $\lambda_a(\mathbf{k},\mathbf{q})$ and $\lambda_{+-}(\mathbf{k},\mathbf{q})$ can be calculated in the continuum model approach following Ref. [6].

The full Hamiltonian is

$$H = \sum_{\mathbf{k};a,\sigma} \xi_a(\mathbf{k}) c^\dagger_{a\sigma}(\mathbf{k}) c_{a\sigma}(\mathbf{k}) + \frac{1}{2}\int \frac{d^2\mathbf{q}}{(2\pi)^2} \sum_{\mathbf{k_1},\mathbf{k_2};a_1,\sigma_1,a_2,\sigma_2} c^\dagger_{a_1,\sigma_1}(\mathbf{k_1}+\mathbf{q}) c^\dagger_{a_2,\sigma_2}(\mathbf{k_2}-\mathbf{q}) c_{a_2,\sigma_2}(\mathbf{k_2}) c_{a_1,\sigma_1}(\mathbf{k_1}) V(\mathbf{q}) \lambda_{a_1}(\mathbf{k_1},\mathbf{q}) \lambda_{a_2}(\mathbf{k_2},-\mathbf{q}) + \frac{1}{2}\int \frac{d^2\mathbf{q}}{(2\pi)^2} \sum_{\mathbf{k_1},\mathbf{k_2};\sigma_1\sigma_2} \left(c^\dagger_{+,\sigma_1}(\mathbf{k_1}+\mathbf{q}) c^\dagger_{-,\sigma_2}(\mathbf{k_2}-\mathbf{q}) c_{+,\sigma_2}(\mathbf{k_2}) c_{-,\sigma_1}(\mathbf{k_1}) V(2\mathbf{K}+\mathbf{q}) \lambda_{+-}(\mathbf{k_1},\mathbf{q}) \lambda_{-+}(\mathbf{k_2},-\mathbf{q}) + \text{H.c.} \right), \quad \text{(B2)}$$

where we use screened Coulomb interaction $V(\mathbf{q}) = \frac{e^2}{2\xi_0\kappa}\frac{1}{q}(1-e^{-qr_0})$. κ is the renormalized factor for dielectric constant. In this paper, we use $\kappa = 8$. r_0 is the screening length for which we use $r_0 = 5a_M \approx 75$ nm.

The first two terms of Eq. (B2) have $\mathrm{SU}(2)_+ \times \mathrm{SU}(2)_- \times \mathrm{U}(1)_v$ symmetry, which means that SU(2) spin of each valley is separately conserved. The third term breaks it further down to $\mathrm{U}(1)_c \times \mathrm{U}(1)_v \times \mathrm{SU}(2)_s$. We expect this term is suppressed by a factor $\frac{a}{a_M} \approx 0.02$ and therefore we only view it as a perturbation.

APPENDIX C: LATTICE MODEL FOR $\Delta_V < 0$ SIDE

For $\Delta_V < 0$, the bands of both valleys are trivial($C = 0$). Therefore there is exponentially localized Wannier orbital for each valley created by

$$\psi^\dagger_a(\mathbf{x_0}) = \frac{1}{\sqrt{N}} \sum_{\mathbf{k}} e^{-i\mathbf{k}\cdot\mathbf{x_0}} e^{i\theta_a(\mathbf{k})} c^\dagger_a(\mathbf{k}). \quad \text{(C1)}$$

$\theta_a(\mathbf{k})$ can be obtained by the standard projection method [50]: $A = \langle \mu_a(\mathbf{k}) | g_a(\mathbf{k}) \rangle$ and $e^{i\theta_a(\mathbf{k})} = A/|A|$. $\mu_a(\mathbf{k})$ is the Bloch wave function for valley a. $g_a(\mathbf{k})$ is an initial ansatz localized in real space. We choose $g_a(\mathbf{k})$ to be the Fourier transformation of

$$|g_a(\mathbf{x})\rangle = e^{-\frac{(\mathbf{x}-\mathbf{x_0})^2}{2\alpha^2}} |\phi_a\rangle, \quad \text{(C2)}$$

where $\alpha = \frac{a_M}{16}$ and $|\phi_a\rangle$ is a constant vector corresponding to sublattices (which can be viewed as pseudospin degree of freedom and for simplicity we assume an ansatz for which the pseudospin is independent of $\mathbf{x}$). The value of $|\phi_a\rangle$ is chosen to optimize the overlap $|\langle \mu_a(\mathbf{k}) | g_a(\mathbf{k}) \rangle|$.

After getting $\theta_a(\mathbf{k})$, we can easily transform the Hamiltonian in Eq. (B2) in terms of real space operator $\psi_a(\mathbf{x})$ with $\mathbf{x} = \mathbf{x_0} + m\mathbf{a_1} + n\mathbf{a_2}$ forming a two-dimensional triangular lattice. $\mathbf{a_1} = a_M(1,0)$ and $\mathbf{a_2} = a_M(\frac{1}{2}, \frac{\sqrt{3}}{2})$.

For the kinetic term, we have

$$H_K = -\sum_{a;m,n,\mathbf{x}} t_a(m,n) \psi^\dagger_a(\mathbf{x} + m\mathbf{a_1} + n\mathbf{a_2}) \psi_a(\mathbf{x}) + \text{H.c.} \quad \text{(C3)}$$

with

$$t_a(m,n) = -\frac{1}{N} \sum_{\mathbf{k}} \xi_a(\mathbf{k}) e^{-i\mathbf{k}\cdot(m\mathbf{a_1}+n\mathbf{a_2})}. \quad \text{(C4)}$$

Similarly we can generate all of four fermion interactions. The second line in Eq. (B2) gives

$$H_V = \frac{1}{2} \sum_{\mathbf{x},\mathbf{R_1},\mathbf{R_2},\mathbf{R_3}} V_{ab}(\mathbf{R_1},\mathbf{R_2},\mathbf{R_3}) \psi^\dagger_{a\sigma_1}(\mathbf{x}) \psi^\dagger_{b\sigma_2} \times (\mathbf{x}+\mathbf{R_1}) \psi_{b\sigma_2}(\mathbf{x}+\mathbf{R_2}) \psi_{a\sigma_1}(\mathbf{x}+\mathbf{R_3}) \quad \text{(C5)}$$

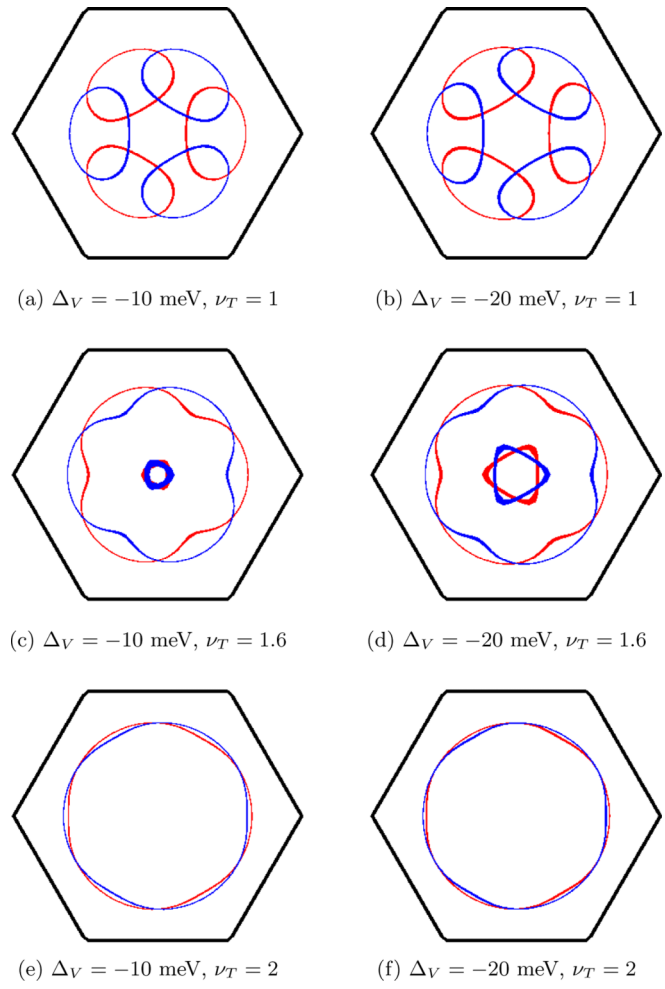

(a) $\Delta_V = -10$ meV, $\nu_T = 1$ (b) $\Delta_V = -20$ meV, $\nu_T = 1$

(c) $\Delta_V = -10$ meV, $\nu_T = 1.6$ (d) $\Delta_V = -20$ meV, $\nu_T = 1.6$

(e) $\Delta_V = -10$ meV, $\nu_T = 2$ (f) $\Delta_V = -20$ meV, $\nu_T = 2$

FIG. 13. Fermi surfaces at $\nu_T = 1$ and $\nu_T = 2$. Red and blue lines denotes the Fermi surface contours for the two different valleys. For $\nu_T = 1$, there are three separate Fermi surfaces related by the C_3 symmetry. When increasing ν_T, there is a Lifshitz transition to an annulus-shape Fermi sea. At $\nu_T = 2$, the Fermi surface is simply a circle for each valley.

with

$$V_{ab}(\mathbf{R_1},\mathbf{R_2},\mathbf{R_3}) = \frac{1}{N^3}\sum_{\mathbf{k_1},\mathbf{k_2},\mathbf{q}}\sum_{a,b} V(\mathbf{q}) e^{-i\theta_a(\mathbf{k_1}+\mathbf{q})} e^{-i\theta_b(\mathbf{k_2}-\mathbf{q})} e^{i\theta_b(\mathbf{k_2})} e^{i\theta_a(\mathbf{k_1})} \lambda_a \times (\mathbf{k_1},\mathbf{q})\lambda_b(\mathbf{k_2},-\mathbf{q}) e^{i(\mathbf{k_2}-\mathbf{q})\cdot\mathbf{R_1}} e^{-i\mathbf{k_2}\cdot\mathbf{R_2}} e^{-i\mathbf{k_1}\cdot\mathbf{R_3}}. \quad \text{(C6)}$$

The dominant term is on-site and nearest-neighbor Hubbard U. The next order is Hund's coupling, as shown in Eq. (6). There are also pair hopping and correlated hopping terms:

$$\sum_{ab}\big(g_{dh}U\psi^\dagger_{a\sigma_1}(\mathbf{x})\psi^\dagger_{b\sigma_2}(\mathbf{x}+\mathbf{a_1})\psi_{b\sigma_2}(\mathbf{x})\psi_{a\sigma_1}(\mathbf{x}) + g_{hh}U\psi^\dagger_{a\sigma_1}(\mathbf{x})\psi^\dagger_{b\sigma_2}(\mathbf{x}+\mathbf{a_1})\psi_{b\sigma_2}(\mathbf{x})\psi_{a\sigma_1}(\mathbf{x}+\mathbf{a_1}) + \text{H.c.}\big). \quad \text{(C7)}$$

These terms $g_{dh}U \sim g_{hh}U \sim 0.02U \approx 0.5$ meV, which is at the same order of Hund's coupling g_hU term in Eq. (6). However, they involve onsite double occupancy, which should be suppressed by the much larger Hubbard U. Therefore as a simplifying approximation we only keep Hund's coupling term and ignore these correlated hopping and pair hopping terms.

Last, we also need to include the third line of Eq. (B2). It turns out that in real space this terms leads to an on-site intervalley Hund's coupling, i.e., J_H term in Eq. (6).

APPENDIX D: $\Delta_V > 0$: $C = \pm 3$ CHERN BANDS

For $\Delta_V > 0$, localized Wannier orbitals for each valley are impossible because of the nonzero Chern number. However, we can have a triangular lattice model with two orbitals per site at the cost that the valley I_z operator can not be on-site. This kind of model was first discussed for the topologically nontrivial bands of the twisted bilayer graphene system [8].

We choose two initial localized ansatz $|g_1\rangle$ and $|g_2\rangle$ centered at a triangular lattice. They are related by the time-reversal transformation. We label valley $+,-$ as 1,2. Then we calculate the following 2×2 matrix: $A_{mn}(\mathbf{k}) = \langle\mu_m(\mathbf{k})|g_n(\mathbf{k})\rangle$ at each momentum point $\mathbf{k}$. This give the following two projected states:

$$\varphi^\dagger_n(\mathbf{x}_0) = \frac{1}{\sqrt{N}}\sum_{\mathbf{k};a} A_{an}(\mathbf{k}) e^{-i\mathbf{k}\cdot\mathbf{x_0}} c^\dagger_a(\mathbf{k}), \quad \text{(D1)}$$

where $m,n = 1,2$ and $c_a(\mathbf{k})$ is the annilation operator of the valley a.

φ_1 and φ_2 create states which are not orthogonal and normalized. We define the following unitary matrix:

$$U(\mathbf{k}) = A(A^\dagger A)^{-\frac{1}{2}}. \quad \text{(D2)}$$

If we do singular value decomposition: $A = ZDW^\dagger$, then

$$U(\mathbf{k}) = ZW^\dagger. \quad \text{(D3)}$$

Then we get Wannier orbitals:

$$\psi^\dagger_n(\mathbf{x}_0) = \frac{1}{\sqrt{N}}\sum_{\mathbf{k};a} e^{-i\mathbf{k}\cdot\mathbf{x_0}} c^\dagger_a(\mathbf{k}) U_{an}(\mathbf{k}). \quad \text{(D4)}$$

It is easy to prove that $|\psi_1\rangle = \psi^\dagger_1(\mathbf{x}_0)|0\rangle$ and $|\psi_2\rangle = \psi^\dagger_2(\mathbf{x}_0)|0\rangle$ are normalized and orthogonal.

We can build our lattice models in terms of operators $\psi_1(\mathbf{x_0}+m\mathbf{a_1}+n\mathbf{a_2})$ and $\psi_2(\mathbf{x_0}+m\mathbf{a_1}+n\mathbf{a_2})$ where $\mathbf{a_1}$ and $\mathbf{a_2}$ are the unit vectors of the corresponding triangular lattice.

Using

$$c_a(\mathbf{k}) = \frac{1}{\sqrt{N}}\sum_{\mathbf{x_0};n} e^{-i\mathbf{k}\cdot\mathbf{x_0}} U_{an}(\mathbf{k})\psi_n(\mathbf{x}_0), \quad \text{(D5)}$$

we can express Eq. (B2) in terms of these ψ_m Wannier operators.

First for kinetic term, we have

$$H_K = -\sum_{i,j}\sum_{m,n} t_{mn}(\mathbf{R})\psi^\dagger_{i;m}\psi_{j;n}, \quad \text{(D6)}$$

where $\mathbf{R} = \mathbf{x_j} - \mathbf{x_i}$.

$$t_{mn}(\mathbf{R}) = \frac{1}{N}\sum_{\mathbf{k};a} U^\dagger_{ma}(\mathbf{k})\xi_a(\mathbf{k})U_{an}(\mathbf{k})e^{-i\mathbf{k}\cdot\mathbf{R}}, \quad \text{(D7)}$$

where $m,n = A$ and B are orbital indexes for each site. $a = +,-$ is valley index. i and j are labels of triangular lattice sites.

We keep intraorbital hopping $t(x,y) = t_{AA}(x\mathbf{a_1}+y\mathbf{a_2})$ and interorbital hopping $t'(x,y) = t_{AB}(x\mathbf{a_1}+y\mathbf{a_2})$. Other components can be generated by the time-reversal transformation: $\psi_{m;i}\to\epsilon_{mn}\psi_{n;i}$, where $\epsilon_{AB} = -\epsilon_{BA} = 1$ while $\epsilon_{AA} = \epsilon_{BB} = 0$.

There is always the following symmetry $t(\mathbf{x}) = t(C_3\mathbf{x}) = t^*(-\mathbf{x}) = t^*(C_6\mathbf{x})$ and $t'(\mathbf{x}) = t'(C_6\mathbf{x})$. The mirror reflection symmetry can not be kept explicitly in the current approach.

$I_z = \sum_{\mathbf{k}} c^\dagger_+(\mathbf{k})c_+(\mathbf{k}) - c^\dagger_-(\mathbf{k})c_-(\mathbf{k})$ can not be implemented as on site operator in the Wannier orbital $\psi_{i;m}$ basis. Instead, we have

$$I_z = \sum_{i,j}\sum_{m,n} t^v_{mn}(\mathbf{R})\psi^\dagger_{i;m}\psi_{j;n} \quad \text{(D8)}$$

Again we have intraorbital hopping $t_V(x,y) = t_{AA}(x\mathbf{a_1}+y\mathbf{a_2})$ and interorbital hopping $t'_V(x,y) = t_{AB}(x\mathbf{a_1}+y\mathbf{a_2})$. The symmetry requirement is $t_V(\mathbf{x}) = t_V(C_6\mathbf{x})$ and $t'_V(\mathbf{x}) = -t'_V(C_6\mathbf{x})$. $t_{BB}(\mathbf{x}) = -t_{AA}(\mathbf{x})$ and $t_{AB}(\mathbf{x}) = -t^*_{BA}(\mathbf{x})$ follow from $TI_zT^{-1} = -I_z$ under time reversal.

Similarly to the $\Delta_V < 0$ case, four fermion interaction can be expressed in terms of Wannier orbital operator $\psi_{i;m}$ in real space:

$$H_V = \frac{1}{2}\sum_{\sigma_1;\sigma_2}\sum_{\mathbf{x},\mathbf{R_1},\mathbf{R_2},\mathbf{R_3}} V_{m_1n_1n_2m_2}(\mathbf{R_1},\mathbf{R_2},\mathbf{R_3})\psi^\dagger_{m_1\sigma_1}(\mathbf{x})\psi^\dagger_{n_1\sigma_2} \times(\mathbf{x}+\mathbf{R_1})\psi_{n_2\sigma_2}(\mathbf{x}+\mathbf{R_2})\psi_{m_2\sigma_1}(\mathbf{x}+\mathbf{R_3}), \quad \text{(D9)}$$

where

$$V_{m_1n_1n_2m_2}(\mathbf{R_1},\mathbf{R_2},\mathbf{R_3}) = \frac{1}{N^3}\sum_{\mathbf{k_1},\mathbf{k_2},\mathbf{q}}\sum_{a,b} V(\mathbf{q})U^*_{am_1}(\mathbf{k_1}+\mathbf{q})U^*_{bn_1}(\mathbf{k_2}-\mathbf{q})U_{bn_2} \times(\mathbf{k_2})U_{am_2}(\mathbf{k_1})\lambda_a(\mathbf{k_1},\mathbf{q})\lambda_b \times(\mathbf{k_2},-\mathbf{q})e^{i(\mathbf{k_2}-\mathbf{q})\cdot\mathbf{R_1}}e^{-i\mathbf{k_2}\cdot\mathbf{R_2}}e^{-i\mathbf{k_1}\cdot\mathbf{R_3}}. \quad \text{(D10)}$$

TABLE III. Tight binding parameters of the kinetic Hamiltonian H_K for $\Delta_V = 50$ meV. t and t' are intraorbital and interorbital hopping parameters in units of meV.

R	(0,0)	(1,0)	(1,1)	(2,1)	(1,2)	(2,0)
t	0	$0.984e^{i0.006\pi}$	-0.836	$0.293e^{-i0.002\pi}$	$0.293e^{i0.002\pi}$	$-0.236e^{i0.021\pi}$
t'	$-0.155e^{-i0.380\pi}$	$0.064e^{-i0.380\pi}$	$-0.082e^{-i0.379\pi}$	$0.026e^{-i0.256\pi}$	$-0.026e^{i0.496\pi}$	$0.027e^{-i0.378\pi}$

Result

We provide a two-orbital model for the $C = \pm 3$ bands following the procedure described above. For simplicity we ignore the trigonal warping term γ_3 of Eq. (A1) for the calculation of $\Delta_V > 0$.

Tight binding parameters for H_K and I_z are listed in Tables III and IV for $\Delta_V = 50$ meV. These tight binding parameters for a two orbital model can reproduce the two valence bands for each spin with Chern number $C = \pm 3$.

One can also write four fermion interactions in terms of these ψ_m operators. We list the dominant interaction terms following the convention of Eq. (D10) in Table V. The dominant term is still the on-site U and the next-nearest-neighbor repulsion U_1. For the $\Delta_V > 0$ side $U = 10$ meV and is only one half of the value at the $\Delta_V < 0$ side. Meanwhile the intersite Hund's coupling and correlated hopping terms are at the order of $0.1U$ instead of $0.01U$ for the $\Delta_V < 0$ side. These are signatures of the Wannier obstruction. In the $\frac{t}{U} \ll 0$ limit for integer fillings, we still expect an insulating ground state. These intersite Hund's coupling, correlated hopping and pair-hopping terms are much larger than the superexchange t^2/U terms and we expect the ground state is decided by these terms. However, the lack of the explicit valley index makes it hard to reliably deal with this lattice model. From Hartree Fock calculations in the momentum space [6] we expect the ground state to be valley polarized for $\nu_T = 1$. However, we do not know how to understand this conclusion from the above lattice model.

APPENDIX E: SPIN-VALLEY MODEL FOR $C = 0$ SIDE

For the $C = 0$ side, to order $t \ll U$, we derive a spin-valley model following the standard approach. There is already a Hund's coupling in the four fermion interaction. Besides, at the order of t^2/U, we get the following superexchange antiferromagnetic term:

$$H_S = \frac{t^2}{U} \sum_{\langle ij \rangle} \sum_{a_1\sigma_1, a_2\sigma_2} \left(e^{i(\varphi^{ij}_{a_1} - \varphi^{ij}_{a_2})} f^\dagger_{i;a_1\sigma_1} f_{i;a_2\sigma_2} f^\dagger_{j;a_2\sigma_2} f_{j;a_1\sigma_1} + \text{H.c.} \right), \tag{E1}$$

where a_1, a_2 are valley indexes and σ_1, σ_2 are spin indexes. We use f instead of c to emphasize that they are neutral degrees of freedom which only carry spin and valley quantum numbers. φ_a is the phase in the nearest-neighbor hopping for valley a. From time reversal, $\varphi^{ij}_+ = -\varphi^{ij}_- = \varphi$.

We label operator $\tau_\mathbf{i} \otimes \sigma_\mathbf{i} = f^\dagger_{i;a_1\sigma_1} \tau_{a_1a_2} \sigma_{\sigma_1\sigma_2} f_{i;a_2\sigma_2}$ with Einstein summation convention. τ_i labels $I, \tau_x, \tau_y, \tau_z$ operator acting on the valley Hilbert space at site i. Similarly σ_i labels I, σ_x, σ_y, and σ_z.

For $a_1 = a_2 = +$ part, we use the following equation:

$$\sum_{\sigma_1\sigma_2} f^\dagger_{i;+\sigma_1} f_{i;+\sigma_2} f^\dagger_{j;+\sigma_2} f_{j;+\sigma_1} = \frac{1}{2} \frac{I + \tau^z_i}{2} \frac{I + \tau^z_j}{2} (I + \sigma_\mathbf{i} \cdot \sigma_\mathbf{j}), \tag{E2}$$

where terms like $\tau\sigma$ refer to tensor products.

Similar for $a_1 = a_2 = -$ part, we have

$$\sum_{\sigma_1\sigma_2} f^\dagger_{i;-\sigma_1} f_{i;-\sigma_2} f^\dagger_{j;-\sigma_2} f_{j;-\sigma_1} = \frac{1}{2} \frac{I - \tau^z_i}{2} \frac{I - \tau^z_j}{2} (I + \sigma_\mathbf{i} \cdot \sigma_\mathbf{j}). \tag{E3}$$

Then $a_1 = +, a_2 = -$ part gives

$$e^{2i\varphi} \sum_{\sigma_1\sigma_2} f^\dagger_{i;+\sigma_1} f_{i;-\sigma_2} f^\dagger_{j;-\sigma_2} f_{j;+\sigma_1} = \frac{1}{2} e^{2i\varphi} \tau^+_i \tau^-_j (1 + \sigma_\mathbf{i} \cdot \sigma_\mathbf{j}). \tag{E4}$$

Similarly $a_1 = -, a_2 = +$ part gives

$$e^{-2i\varphi} \sum_{\sigma_1\sigma_2} f^\dagger_{i;-\sigma_1} f_{i;+\sigma_2} f^\dagger_{j;-\sigma_2} f_{j;+\sigma_1} = \frac{1}{2} e^{-2i\varphi} \tau^-_i \tau^+_j (1 + \sigma_\mathbf{i} \cdot \sigma_\mathbf{j}). \tag{E5}$$

Summing the above four terms together, we get the spin-valley coupling from the superexchange:

$$\frac{t^2}{2U} \sum_{\langle ij \rangle} \big((I + \tau_\mathbf{i} \cdot \tau_\mathbf{j})(I + \sigma_\mathbf{i} \cdot \sigma_\mathbf{j}) - (1 - \cos 2\varphi_{ij}) \big(\tau^x_i \tau^x_j + \tau^y_i \tau^y_j \big)(1 + \sigma_\mathbf{i} \cdot \sigma_\mathbf{j}) + \sin 2\varphi_{ij} \big(\tau^x_i \tau^y_j - \tau^y_i \tau^x_j \big)(I + \sigma_\mathbf{i} \cdot \sigma_\mathbf{j}) \big), \tag{E6}$$

where the second and the third terms break SU(4) symmetry to $\mathrm{SU}(2)_+ \times \mathrm{SU}(2)_- \times \mathrm{U}(1)_v$.

TABLE IV. Tight binding parameters of the valley operator I_z for $\Delta_V = 50$ meV. t and t' are intraorbital and interorbital hopping parameters in units of meV.

R	(0,0)	(1,0)	(1,1)	(2,1)	(1,2)	(2,0)
t_V	0.347	0.189	-0.133	0.020	0.019	-0.090
t'_V	0	$0.252e^{i0.121\pi}$	$-0.172e^{-i0.380\pi}$	$-0.044e^{i0.493\pi}$	$0.044e^{-i0.255\pi}$	$0.038e^{i0.125\pi}$

TABLE V. Interaction parameters (in units of meV) for $\Delta_V = 50$ meV. The list is not complete. Other terms can be generated from Hermitian conjugation and time reversal transformation.

m_1	n_1	n_2	m_2	$\mathbf{R_1}$	$\mathbf{R_2}$	$\mathbf{R_3}$	$V_{m_1n_1n_2m_2}(\mathbf{R_1}, \mathbf{R_2}, \mathbf{R_3})$	Comments
A	A	A	A	(0,0)	(0,0)	(0,0)	9.39	on-site U
A	A	A	A	(1,0)	(1,0)	(0,0)	4.09	nearest-neighbor U
A	A	A	A	(1,0)	(0,0)	(0,0)	$1.08e^{-i0.008\pi}$	correlated hopping
A	A	A	A	(1,0)	(0,0)	(1,0)	0.65	intersite Hund's
A	A	A	A	(1,0)	(1,0)	(0,0)	0.50	pair hopping
A	B	B	A	(0,0)	(0,0)	(0,0)	9.39	on-site U
A	B	B	A	(1,0)	(1,0)	(0,0)	4.09	nearest-neighbor U
A	B	B	A	(1,0)	(0,0)	(0,0)	$1.08e^{i0.008\pi}$	correlated hopping
A	B	B	A	(1,0)	(0,0)	(1,0)	0.50	intersite Hund's
A	B	B	A	(1,0)	(1,0)	(0,0)	0.65	pair hopping
A	B	A	B	(0,0)	(0,0)	(0,0)	0.15	
A	B	A	B	(1,0)	(1,0)	(0,0)	$0.017e^{i0.77\pi}$	
A	B	A	B	(1,0)	(0,0)	(0,0)	$0.07e^{i0.42\pi}$	
A	B	A	B	(1,0)	(0,0)	(1,0)	0.73	
A	B	A	B	(1,0)	(1,0)	(0,0)	0.73	
A	A	A	B	(0,0)	(0,0)	(0,0)	$0.55e^{i0.58\pi}$	
A	A	A	B	(1,0)	(1,0)	(0,0)	$0.16e^{i0.68\pi}$	
A	A	A	B	(1,0)	(0,0)	(0,0)	$0.07e^{i0.70\pi}$	
A	A	A	B	(1,0)	(0,0)	(1,0)	$0.13e^{0.018\pi}$	
A	A	A	B	(1,0)	(1,0)	(0,0)	$0.147e^{-i0.78\pi}$	
A	A	B	A	(0,0)	(0,0)	(0,0)	$0.55e^{i0.58\pi}$	
A	A	B	A	(1,0)	(1,0)	(0,0)	$0.16e^{i0.54\pi}$	
A	A	B	A	(1,0)	(0,0)	(0,0)	$0.79e^{i0.078\pi}$	
A	A	B	A	(1,0)	(0,0)	(1,0)	$0.147e^{-i0.78\pi}$	
A	A	B	A	(1,0)	(1,0)	(0,0)	$0.147e^{-i0.78\pi}$	

[1] E. M. Spanton, A. A. Zibrov, H. Zhou, T. Taniguchi, K. Watanabe, M. P. Zaletel, and A. F. Young, Science **360**, 62 (2018).

[2] Y. Cao, V. Fatemi, A. Demir, S. Fang, S. L. Tomarken, J. Y. Luo, J. D. Sanchez-Yamagishi, K. Watanabe, T. Taniguchi, E. Kaxiras *et al.*, Nature (London) **556**, 80 (2018).

[3] Y. Cao, V. Fatemi, S. Fang, K. Watanabe, T. Taniguchi, E. Kaxiras, and P. Jarillo-Herrero, Nature (London) **556**, 43 (2018).

[4] G. Chen, L. Jiang, S. Wu, B. Lv, H. Li, K. Watanabe, T. Taniguchi, Z. Shi, Y. Zhang, and F. Wang, Nat. Phys. **15**, 237 (2019).

[5] M. Yankowitz, S. Chen, H. Polshyn, Y. Zhang, K. Watanabe, T. Taniguchi, D. Graf, A. F. Young, and C. R. Dean, Science **363**, 1059 (2019).

[6] Y.-H. Zhang, D. Mao, Y. Cao, P. Jarillo-Herrero, and T. Senthil, Phys. Rev. B **99**, 075127 (2019).

[7] B. L. Chittari, G. Chen, Y. Zhang, F. Wang, and J. Jung, Phys. Rev. Lett. **122**, 016401 (2019).

[8] H. C. Po, L. Zou, A. Vishwanath, and T. Senthil, Phys. Rev. X **8**, 031089 (2018).

[9] R. Bistritzer and A. H. MacDonald, Proc. Natl. Acad. Sci. U.S.A. **108**, 12233 (2011).

[10] G.-Y. Zhu, T. Xiang, and G.-M. Zhang, arXiv:1806.07535.

[11] M. Imada, A. Fujimori, and Y. Tokura, Rev. Mod. Phys. **70**, 1039 (1998).

[12] T. Senthil, Phys. Rev. B **78**, 045109 (2008).

[13] L. Zou, H. C. Po, A. Vishwanath, and T. Senthil, Phys. Rev. B **98**, 085435 (2018).

[14] J. Ahn, S. Park, and B.-J. Yang, Phys. Rev. X **9**, 021013 (2019).

[15] Z. Song, Z. Wang, W. Shi, G. Li, C. Fang, and B. A. Bernevig, arXiv:1807.10676.

[16] H. C. Po, L. Zou, T. Senthil, and A. Vishwanath, arXiv:1808.02482.

[17] D. Xiao, M.-C. Chang, and Q. Niu, Rev. Mod. Phys. **82**, 1959 (2010).

[18] D. Xiao, W. Yao, and Q. Niu, Phys. Rev. Lett. **99**, 236809 (2007).

[19] M. Koshino, Phys. Rev. B **84**, 125427 (2011).

[20] L. Ju, L. Wang, T. Cao, T. Taniguchi, K. Watanabe, S. G. Louie, F. Rana, J. Park, J. Hone, F. Wang *et al.*, Science **358**, 907 (2017).

[21] K. Komatsu, Y. Morita, E. Watanabe, D. Tsuya, K. Watanabe, T. Taniguchi, and S. Moriyama, Sci. Adv. **4**, eaaq0194 (2018).

[22] B. Huang, G. Clark, E. Navarro-Moratalla, D. R. Klein, R. Cheng, K. L. Seyler, D. Zhong, E. Schmidgall, M. A. McGuire, D. H. Cobden *et al.*, Nature (London) **546**, 270 (2017).

[23] Z. Zhu and S. R. White, Phys. Rev. B **92**, 041105(R) (2015).

[24] W.-J. Hu, S.-S. Gong, W. Zhu, and D. N. Sheng, Phys. Rev. B **92**, 140403(R) (2015).

[25] S.-S. Gong, W. Zhu, J.-X. Zhu, D. N. Sheng, and K. Yang, Phys. Rev. B **96**, 075116 (2017).

[26] O. I. Motrunich, Phys. Rev. B **72**, 045105 (2005).
[27] H. R. Krishnamurthy, C. Jayaprakash, S. Sarker, and W. Wenzel, Phys. Rev. Lett. **64**, 950 (1990).
[28] Y. Kurosaki, Y. Shimizu, K. Miyagawa, K. Kanoda, and G. Saito, Phys. Rev. Lett. **95**, 177001 (2005).
[29] T. Furukawa, K. Kobashi, Y. Kurosaki, K. Miyagawa, and K. Kanoda, Nat. Commun. **9**, 307 (2018).
[30] Y. Zhou, K. Kanoda, and T.-K. Ng, Rev. Mod. Phys. **89**, 025003 (2017).
[31] T. Furukawa, K. Miyagawa, H. Taniguchi, R. Kato, and K. Kanoda, Nat. Phys. **11**, 221 (2015).
[32] K. Kanoda and R. Kato, Annu. Rev. Condens. Matter Phys. **2**, 167 (2011).
[33] H. Isobe, N. F. Yuan, and L. Fu, Phys. Rev. X **8**, 041041 (2018).
[34] Y.-Z. You and A. Vishwanath, arXiv:1805.06867.
[35] H. Morita, S. Watanabe, and M. Imada, J. Phys. Soc. Jpn. **71**, 2109 (2002).
[36] H.-Y. Yang, A. M. Läuchli, F. Mila, and K. P. Schmidt, Phys. Rev. Lett. **105**, 267204 (2010).
[37] D. N. Sheng, O. I. Motrunich, and M. P. A. Fisher, Phys. Rev. B **79**, 205112 (2009).
[38] A. Szasz, J. Motruk, M. P. Zaletel, and J. E. Moore, arXiv:1808.00463.
[39] S. Florens and A. Georges, Phys. Rev. B **70**, 035114 (2004).
[40] S.-S. Lee and P. A. Lee, Phys. Rev. Lett. **95**, 036403 (2005).
[41] R. V. Mishmash, I. González, R. G. Melko, O. I. Motrunich, and M. P. A. Fisher, Phys. Rev. B **91**, 235140 (2015).
[42] W. Witczak-Krempa, P. Ghaemi, T. Senthil, and Y. B. Kim, Phys. Rev. B **86**, 245102 (2012).
[43] O. I. Motrunich, Phys. Rev. B **73**, 155115 (2006).
[44] D. Chowdhury, I. Sodemann, and T. Senthil, Nat. Commun. **9**, 1766 (2018).
[45] I. Sodemann, D. Chowdhury, and T. Senthil, Phys. Rev. B **97**, 045152 (2018).
[46] Z. Xiang, Y. Kasahara, T. Asaba, B. Lawson, C. Tinsman, L. Chen, K. Sugimoto, S. Kawaguchi, Y. Sato, G. Li *et al.*, Science **362**, 65 (2018).
[47] T. Senthil and P. A. Lee, Phys. Rev. Lett. **103**, 076402 (2009).
[48] T. Senthil, M. Vojta, and S. Sachdev, Phys. Rev. B **69**, 035111 (2004).
[49] E. McCann and M. Koshino, Rep. Prog. Phys. **76**, 056503 (2013).
[50] N. Marzari, A. A. Mostofi, J. R. Yates, I. Souza, and D. Vanderbilt, Rev. Mod. Phys. **84**, 1419 (2012).